Renewable Energy 264 (2026) 125508

Contents lists available at ScienceDirect

Renewable Energy

journal homepage: www.elsevier.com/locate/renene

Effects of photovoltaic module on wind dynamics over water surface for aquavoltaic applications

Haoran Chang [a,1], Peixin Dong [b,1], Xin Wei [a], Liutao Chen [b], Hui Tang [a], Zhe Wang [b], Su Guo [c], Mengying Li [a,*]

[a] Department of Mechanical Engineering & Research Institute for Smart Energy, The Hong Kong Polytechnic University, Hong Kong Special Administrative Region
[b] Department of Civil and Environmental Engineering, Hong Kong University of Science and Technology, Hong Kong Special Administrative Region
[c] School of Renewable Energy, Hohai University, Nanjing, China

ARTICLE INFO

Keywords:
Aquavoltaic system
3-D numerical modeling
Wind dynamics over water surface
PV module configurations
Semi-empirical formula

ABSTRACT

The increasing scarcity of available land has accelerated the adoption of aquavoltaic systems; however, concerns about their environmental impacts are growing. Specifically, the influence of photovoltaic (PV) modules on water surface wind speed remains inadequately explored. To address this knowledge gap, a three-dimensional numerical model is developed to systematically investigate the effects of module tilt angle (β), height (h), incoming wind speed (u_a), and wind direction (θ) on the relative wind speed (u_r) over water surface, compared to a baseline case without PV modules. Detailed flow field analyses reveal that the south-facing PV module generates distinct wind flow patterns: under southerly winds, channeling effects enhance near-surface flow, while under northerly winds, competing channeling and blockage effects suppress it. Variations in u_a produce changes of less than 1% in u_r, confirming their negligible influence. A critical installation height of $h = 1.5$ m is identified, above which aerodynamic disturbances become insignificant. Below this threshold, flow disturbances intensify with increasing β, with u_r peaking at 1.25 under south winds and decreasing to 0.85 under north winds at $h = 0.5$ m and $\beta = 80°$. Additionally, a semi-empirical formula for u_r is derived by incorporating the equivalent wind speed into a power-law expression and calibrating its coefficients through regression, achieving estimation errors of less than 4%. Finally, the relationship between u_r and the cooling of the PV modules is established, including their impact on the local microclimate. Based on this, the optimal ventilation height is proposed, along with the corresponding variations in water surface evaporation rates and convective heat transfer coefficients caused by changes in wind speed. These findings provide a generalized analytical tool for quantifying PV-induced airflow modifications and support the environmentally informed design of aquavoltaic systems.

1. Introduction

The acceleration of global climate change has brought renewable energy technologies to the forefront of the energy transition [1]. Among the diverse range of renewable technologies, photovoltaic (PV) systems stand out due to the universal availability of solar resources and their advanced technological maturity [2]. However, the expansion of conventional land-based PV (LPV) is increasingly constrained by spatial and environmental bottlenecks [3,4]. The extensive land requirements frequently conflict with agriculture and urbanization while simultaneously posing a risk of ecological disturbance in sensitive habitats [5]. Furthermore, terrestrial installations are inherently susceptible to temperature-induced power degradation via the negative temperature coefficient of photovoltaic materials.

To circumvent land-use limitations and alleviate thermal inefficiencies, aquavoltaic systems have gained traction as an innovative solution, particularly in coastal regions with high population density and electricity demand [6]. By utilizing water bodies, these systems avoid expensive land acquisition costs while leveraging the natural cooling effect of water to enhance PV performance and reduce operational expenses [7]. Technologically, aquavoltaics deployed over water surfaces can be broadly categorized into two main types: floating photovoltaic (FPV), which employs floating structures to support panels; and pile-supported photovoltaic (SPV) systems, which employ fixed piles to support panels [8]. From the environmental impact perspective, FPV systems inevitably alter aquatic microclimates by shading the water surface and obstructing air–water mass exchange.

* Corresponding author.
E-mail address: mengying.li@polyu.edu.hk (M. Li).
[1] These two authors contributed equally to this work.

https://doi.org/10.1016/j.renene.2026.125508
Received 22 September 2025; Received in revised form 27 February 2026; Accepted 28 February 2026
Available online 6 March 2026

They not only attenuate solar irradiance but also impede surface aeration, leading to suppressed evaporation rates and diminished dissolved oxygen concentrations, which, in turn, reshape underwater habitats and affect aquatic biodiversity [9]. From the perspective of module operating temperature, the thermal advantage of traditional FPV is highly context-dependent rather than intrinsic [7]. Although the evaporative cooling of water is theoretically beneficial, the low clearance above the water often impedes air circulation. This obstruction leads to reduced wind velocity across the module surfaces, thereby diminishing the efficiency of convective heat dissipation.

To mitigate such issues, SPV or elevated FPV systems with partial water surface coverage are increasingly preferred in practice [10], as they promote air circulation while minimizing disruption to natural aquatic environments. Nevertheless, elevated PV modules can still drastically alter local wind dynamics, modifying airflow patterns and thereby affecting the convective cooling of the modules [11] and the evaporation rate of the water [12]. This aerodynamic interaction is complex and varies substantially depending on the PV configuration and the prevailing on-site wind conditions. To quantify these physical processes, field measurements have traditionally been employed to capture fundamental wind characteristics [13], whereas Computational Fluid Dynamics (CFD) simulations offer deeper insights into wind-PV interactions by enabling high-resolution modeling of airflow [14].

The critical role of wind-induced convective heat transfer in regulating PV module temperature has been extensively studied, both experimentally and numerically [15]. In dynamic outdoor environments, the cooling efficiency is highly influenced by the fluctuating wind field and the specific mounting positions of the PV modules, leading to spatial variations in thermal regulation that directly impact power generation. Consequently, increasing attention is being paid to the aerodynamic response of PV systems, specifically investigating how varying wind speeds and directions interact with the PV module. For example, Vasel and Iakovidis [16] analyzed PV plant field data based on wind direction, revealing that south-facing PV modules consistently produce more electricity during southerly wind events compared to northerly winds. Kaplani and Kaplanis [17] experimentally demonstrated a strong correlation between wind speed, wind direction, PV module tilt angle, and temperature, emphasizing that numerical models must account for the wind's incident angle relative to the module when computing convective heat transfer coefficients. Wilson and Paul [18] used CFD modeling to study convective flow within the narrow gap between PV panels and the roof surface, revealing that larger air gaps and steeper tilt angles enhance heat dissipation.

A similar constraint is observed in aquavoltaic systems, where installation heights are often restricted to ensure structural stability against high wind loads on open water [19]. Kjeldstad et al. [20]'s field measurements indicate that restricted airflow beneath panels close to the water surface may reduce cooling efficiency compared to LPV systems. Preliminary CFD simulations further showed that wind-driven cooling depends on wind direction. Peters and Nobre [21] reported that at noon, the temperature of the FPV module could be up to 9 °C higher than LPV. Their mathematical model suggests that water only indirectly influences the thermal balance of FPV systems, whereas wind speed and module height serve as primary factors affecting PV cooling performance in areas with overall low wind speeds. More recently, Ramanan et al. [22] found that a 0.25 m-high FPV system provided a cooling advantage over a 0.8 m-high LPV only at sunrise, concluding that improved air ventilation offers greater benefits to FPV systems than to LPV. Ramanan et al. [23] developed a two-dimensional (2-D) CFD model to analyze the combined effects of height and tilt angle on wind-driven heat transfer in a stand-alone FPV system. The velocity contour plots demonstrated that the higher elevation of the LPV system, compared to FPV, led to increased wind speeds at the module edges. This effect is amplified at steeper tilt angles, thereby explaining the disparities in ventilation and heat dissipation performance between the two systems. However, 2-D simulations neglect three-dimensional (3-D) vortex structures and directional wind variations, resulting in substantial deviations from real-world conditions. Although the airflow blockage effect associated with low PV installation heights has been widely acknowledged, it lacks a standardized evaluation metric and detailed quantification. Thus, investigations of wind behavior beneath the PV panels and over the water surface are essential for optimizing thermal management and enhancing renewable energy yields in aquavoltaic systems.

The implications of airflow beneath the PV module go beyond convective heat dissipation; they also play a significant role in profoundly altering the site's microclimate including water evaporation rate and temperature [13]. In aquavoltaic systems, water functions not only as a mounting surface but also as a dynamic ecosystem that is highly sensitive to microclimatic variations. Altered wind patterns directly affect evaporation rates and water surface energy balance, making ecological considerations – particularly the effects of layout and structural parameters on aquatic environments – even more important for achieving environmental benefits. For example, Vidović et al. [24] provided a comprehensive review of cases where FPV systems were employed to manage water evaporation, noting that evaporation rates increase with stronger wind conditions. Baradei and Sadeq [25] employed a mathematical model that accounted for wind effects to determine the optimal coverage area of floating PV panels without affecting water quality. Hamedani et al. [26] pointed out that the obstruction of natural air circulation by PV modules can lead to increased water temperatures. Château et al. [27] developed a mathematical model to assess the ecological effects of PV coverage, stating that wind speed is critical for aquatic habitats as it regulates air–water mass exchange and dissolved oxygen (DO) levels. These processes are largely governed by turbulence derived from the wind stream flowing directly above the water surface, which is crucial for the survival of aquatic organisms [28]. It is evident that airflow dynamics in the near-water region are a critical component of the microclimate in aquavoltaic systems; yet, they remain inadequately considered in existing analytical models. Notably, evaporation estimates often rely on undisturbed ambient wind speeds combined with empirical coefficients to approximate the impact of PV panels [29]. While the significant impact of module-induced wind speed variations on water thermal properties has been acknowledged, discussions remain confined to scenarios involving fully covered floating platforms [30]. Therefore, investigating wind speed over the water surface is essential to addressing these limitations and holds significant potential for clarifying broader environmental impacts in aquavoltaic systems.

In summary, the interplay between the geometric configuration of PV modules and ambient wind conditions governs both ventilation efficiency and water surface turbulence, exerting profound implications for power generation and the aquatic environment. Existing studies have recognized the importance of under-panel airflow and provided valuable case-specific insights through experimental and numerical analyses. However, flow characteristics under different system configurations remain insufficiently explored, and a generalized framework for reliably estimating near-water wind speed variations has yet to be developed. To address these identified research gaps, this study employs a 3-D RANS turbulence model to conduct a steady-state flow field analysis of a standalone aquavoltaic system. The proposed model provides accurate and cost-effective estimations of airflow dynamics above the water surface by utilizing variations in relative wind speed to evaluate under-panel ventilation quality and quantify the associated environmental impacts across different module positions and wind conditions. The key contributions of this work are summarized as follows:

- A high-fidelity CFD model is developed to simulate the wind field over the water surface perturbed by the PV module. The model incorporates variations in physical properties between land and water surfaces and resolves near-wall flows for precise characterization of the boundary layer.

- The effects of module tilt angle, installation height, ambient wind speed, and wind direction on the near-water wind field are systematically investigated. By analyzing the underlying airflow dynamics, the interrelationships among these parameters are elucidated.
- A semi-empirical formula is derived to estimate the relative wind speed within the velocity boundary layer compared to undisturbed conditions. Systematic trends in the coefficients are revealed by fitting simulation data across various wind directions, resulting in a generalized model adaptable to diverse system configurations and environmental inputs.
- The optimal ventilation heights for varying wind directions are proposed by linking relative wind speed to practical scenarios, where the variations in water surface evaporation rates and convective heat transfer coefficients are quantitatively evaluated.

The subsequent sections are organized as follows: Section 2 details the development of the 3-D numerical model and the simulation framework. Section 3 systematically analyzes the impact of PV module placement on near-water airflow fields under varying wind conditions, and introduces an empirical formula to provide insights for practical implications. Finally, Section 4 summarizes the key findings of this study. The Appendix provides the derivation of the empirical formula, the grid convergence test, the experimental validation of the model, and the justification for the modeling assumptions.

2. Methodology

2.1. Problem description

PV modules installed in natural environments alter local airflow patterns, leading to the formation of unique microclimates with distinct temperature, humidity, and wind characteristics. Structure-based aquavoltaic systems typically utilize a dual-pillar supporting frame to enhance stability and minimize direct contact with the water surface. Given their slender profile and span-wise arrangement, these structures generate negligible airflow disturbance, allowing aerodynamic analyses to focus exclusively on the PV module. This study focuses on the investigations of such fixed aquavoltaic systems, as illustrated in Fig. 1. The airflow around the PV module and the water surface can be classified into six distinct regions based on local flow characteristics [31,32]. Particular attention is given to the coupled flow near the water surface, which is influenced by multiple interacting factors.

(I) Free flow: airflow remains unaffected by the PV module, while the boundary layer retains the original kinematic properties of the free stream.

(II) Edge flow: the flow transitions from constrained to free shear around the edges of the PV module.

(III) Separated flow: as airflow encounters the PV module's leading edge, wall friction and adverse pressure gradients diminish the boundary layer's velocity gradient, triggering downstream backflow.

(IV) Wake flow: after separation, rotating vortex structures form in the low-pressure wake behind the module, producing unstable turbulent zones.

(V) Boundary layer flow: viscous effects dominate flows near the ground and the water surface.

(VI) Coupled flow: the intricate near-surface flow within the boundary layer arises from the interplay of boundary layer dynamics, edge effects, and flow separation.

2.2. Simulation framework and parameter configurations

The simulation framework is implemented in COMSOL Multiphysics, enabling detailed analysis of the wind field. A 3-D numerical model is developed, which includes a free-air domain, the ground, a water surface, and a PV module. To establish a universal criterion for cross-scale comparison, the PV module and the water surface are normalized to a consistent length scale, ensuring equivalent coverage over water. At the same time, their original physical dimensions (in meters) are preserved to prevent scaling errors [33].

The aerodynamic disturbance is influenced by several geometric properties, including panel thickness and surface roughness. Accordingly, representative parameter values are utilized as model inputs. As illustrated in Fig. 2(a), the water surface measures 1 m × 1 m and is centrally positioned within the computational domain. Similarly, Fig. 2(b) depicts the PV module, which features a cubic geometry with dimensions of 1 m in length (L), 1 m in width (W), and 0.002 m in thickness. This configuration represents a typical bifacial solar panel encased in an anodized aluminum alloy frame. The layered structure between the glass panels is modeled sequentially using their actual dimensions, in alignment with the experimental setup. To resolve the thin profile of the PV module, a locally refined mesh is employed to accurately capture flow field variations in the near-module region.

The primary objective of the numerical study is to quantify the effects of the PV module on the wind field near the water surface and to investigate how these effects vary under different environmental conditions and PV installation configurations. Accordingly, simulations are conducted with varying PV installation heights, tilt angles, wind speeds, and wind directions.

The simulation cases are meticulously configured to detect subtle effects arising from parameter variations, based on a combination of (i) existing literature, (ii) realistic environmental and engineering constraints, and (iii) the objective of ensuring the general applicability of the present study rather than site-specific optimization.

The installation height, h, defined as the minimum vertical clearance between the PV module and the water surface, strongly affects under-panel ventilation, recirculation, and wake development. The value of 0.5 m represents near-surface constrained flow conditions, whereas increasing elevation enhances airflow penetration and modifies both convective cooling and aerodynamic loading. Additionally, studies on agrivoltaic systems indicate that installation heights exceeding 2 m are typically required to facilitate operation and maintenance [34]. Thus, the PV installation height is selected from 0.5 m to 3 m. The tilt-angle, β, ranges from 0° to 80° to provide generalized insights into PV performance across diverse aerodynamic and thermal conditions, rather than location-specific optimization [35]. The upper bound is justified by environmental considerations such as shading, while a 10° increment ensures sufficient analytical resolution without excessive computational cost. The low-to-moderate wind speeds (1 m/s, 2 m/s, and 4 m/s) are selected to enhance convective cooling and define the PV thermal response under realistic ambient conditions, which capture the primary thermal–aerodynamic response of the PV–air interaction [36]. The wind direction, θ, ranging from north (0°) to south (180°), is selected to encompass all non-redundant inflow conditions for a single PV panel, considering geometric symmetry, as wind-induced pressure distribution and flow structures around PV arrays are highly sensitive to wind direction [37]. In total, 738 simulation cases are conducted, as summarized in Table 1.

Airflow variations near the water surface are quantified by the mean wind speed within the velocity boundary layer, defined as the vertical distance from the surface to the height at which the velocity reaches 99% of the free-stream value. The boundary layer thickness, δ, is estimated using the momentum integral approximation [38] as follows:

$$\delta = \frac{0.383x}{\mathrm{Re}^{1/5}} \tag{1}$$

Here, the Reynolds number (Re) is calculated using the distance from the air inlet to the water surface as the characteristic length x. It should be noted that this empirical formula performs well in typical engineering applications; however, its primary applicability is limited

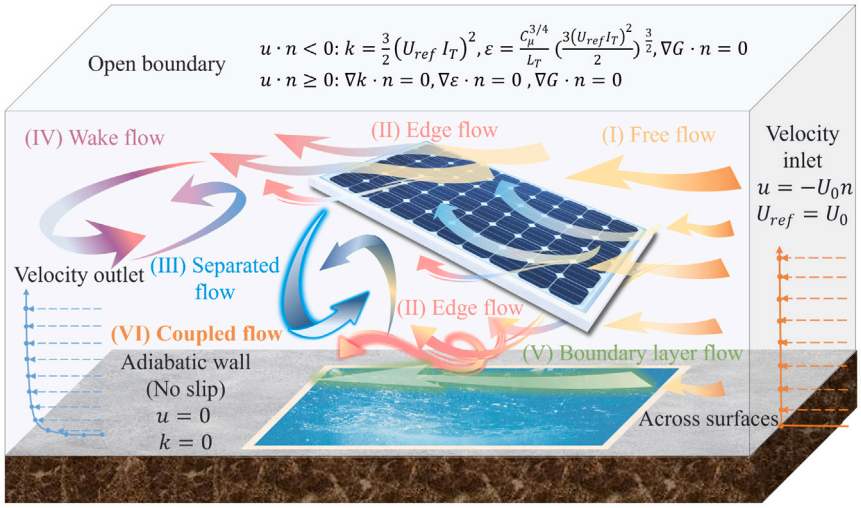

Fig. 1. Airflow patterns around a standalone SPV system.

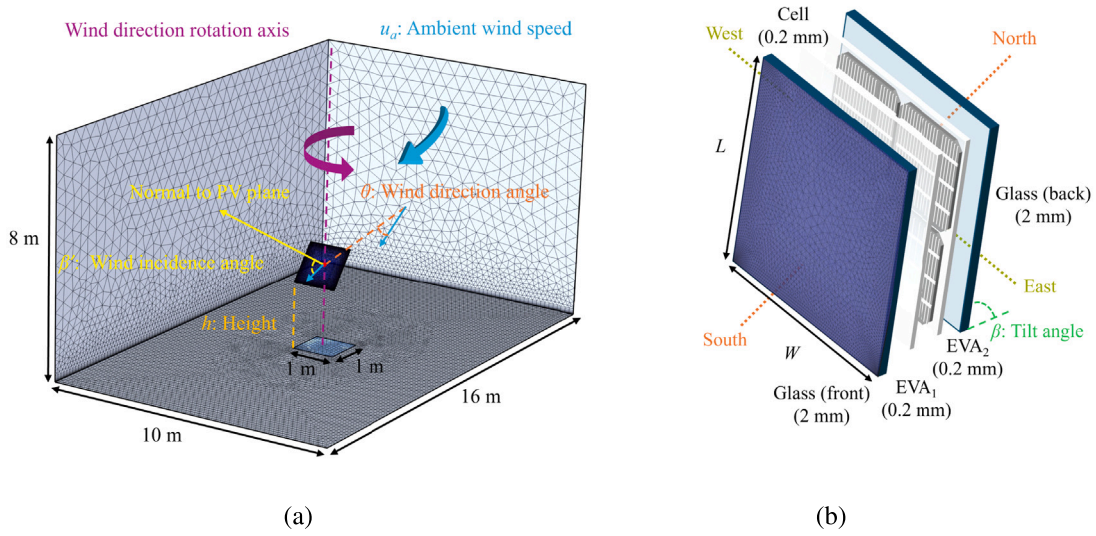

Fig. 2. Geometry of the modeling domain with the illustrated mesh scheme, dimensions, and key variables. (a) Computational domain; (b) PV module.

Table 1
Summary of simulation cases.

Parameter	Symbol	Values	Notes
PV tilt angle (°)	β	0, 10, 20, 30, 40, 50, 60, 70, 80	Common PV installation tilt angle ranges.
PV height (m)	h	0.5, 1, 1.5, 2, 2.5, 3	All heights for 2 m/s wind speed; 4 heights (0.5, 1, 2, 3 m) for 1 m/s and 4 m/s wind speed.
Ambient wind speed (m/s)	u_a	1, 2, 4	Representative conditions (non-extreme conditions)
Wind direction angle (°)	θ	0, 45, 90, 112.5, 135, 157.5, 180	112.5° and 157.5° are simulated only with 2 m/s wind speed for correlation analysis.
Total Cases	**738**		

to moderate Reynolds numbers ranging from 5×10^5 to 10^7, with the surface assumed to be hydraulically smooth. These applicability conditions will be further discussed in subsequent sections to demonstrate the validity of the formula used in this study. Based on this, the boundary layer thickness δ is calculated to be approximately 21 cm.

Given the analogous flow-altering behavior of the PV module and mechanical windbreaks [39], the relative wind speed (u_r) is introduced to quantify the aerodynamic impact of PV configurations, as defined by Eq. (2):

$$u_r = \frac{u_{\mathrm{PV}}}{u_{\mathrm{natural}}} \tag{2}$$

where u_{PV} represents the average wind speed within the velocity boundary layer above the water surface when the PV module is installed, and u_{natural} refers to the average wind speed within the same region when the module is absent.

2.3. Computational domain and assumptions

In numerical simulations, determining the size of the computational domain requires balancing two critical criteria: accuracy, which ensures that the results are independent of domain boundaries, and efficiency, which minimizes computational costs. In this study, the air domain is defined with dimensions of 16 m × 10 m × 8 m, based on the following considerations:

- The width and height of the air domain are determined to ensure simulation reliability by evaluating the blockage effect induced by the PV module. The blockage ratio, defined as the projected area of the module divided by the cross-sectional area of the domain (width × height), is maintained below 1%, which is well below the recommended threshold of 3% [40].
- The length of the computational domain is determined to ensure fully developed flow over the water surface. Consequently, the inlet distance is set to exceed five times the chord length of the PV module [41].
- To ensure consistency in simulations, the same domain dimensions are applied across all cases, with the domain height adjusted based on the maximum values of β and h.
- To ensure that the domain dimensions are adequate for fully developed turbulent airflow over the water surface, Re is calculated using the lowest wind speed, taking the distance from the velocity inlet to the water surface as the characteristic length. Compared to the critical threshold of 5×10^5 for turbulent flow over a flat plate [42], the resulting $\mathrm{Re} = 5.1 \times 10^5$ confirms that the airflow is fully turbulent. Furthermore, this value lies within the applicability range of Eq. (1), validating its suitability for use.

The following assumptions are made to reduce computational complexity and uncertainty while preserving the accuracy of the simulation results:

- The supporting pillar beneath the PV module is neglected.
- The ambient air, water, and PV temperatures are assumed to be constant, while neglecting the influence of buoyancy and density variations on wind speed (See Appendix D.1 for justifications).
- The system configuration is modeled as a single PV module or approximated as an isolated single row, thereby excluding inter-row aerodynamic interference in large-scale PV arrays (See Appendix D.2 for justifications).
- The water and ground surfaces are modeled as 2-D planes at the same elevation, neglecting waves, water ripples, terrain variations, vapor transport, and 3-D hydrodynamic effects.
- The aluminum alloy frame of the PV module is represented as 2-D surfaces occupying the four edges of the PV module.

2.4. Governing equations, boundary conditions and solver

To model turbulence, RANS equations offer superior computational efficiency. This approach has been extensively applied in PV-wind interaction research, providing reliable results while minimizing computational costs [13]. Consequently, RANS is adopted in this work, effectively capturing wake structures, peak locations, and essential vortex features under flow perturbations [43]. Steady-state simulations are employed in this study, as the inlet wind boundary conditions remain constant throughout the computation. Under these conditions, the flow field quickly reaches a stable equilibrium, with minimal changes in velocity, pressure, and turbulence over time. This approach effectively captures key flow features – similar to time-averaged transient results – while reducing computational demands without loss of accuracy [44].

The standard k-ε model is one of the most widely adopted approaches within the RANS framework, demonstrating robustness in estimating mean wind speed distributions during steady-state simulations, and it has been extensively validated [45]. To accurately capture viscous-dominated flow behaviors, the low-Re k-ε model with a damping function is applied in the near-wall regions. For further validation, a comparative analysis with the Shear Stress Transport (SST) k-ω model demonstrates consistent near-surface wind speed predictions, reinforcing the robustness of the numerical approach. Ultimately, the low-Re k-ε model is selected for its superior performance in resolving low-speed separated flows and near-wall effects. Additionally, to capture velocity gradients and minimize errors due to mesh density variations near the ground and water surfaces, a refined mesh that extends from the surface to the velocity boundary layer is used. The first grid layer adjacent to the surface is precisely placed within the viscous sublayer, ensuring the dimensionless wall distance y^+ remains ≤ 1. This approach thereby satisfies the stringent resolution requirements for low-Re simulations.

The flow field in the open-air domain can be numerically solved using the general governing equations of fluid dynamics, which consist of the 3-D Navier–Stokes equations that embody conservation principles:

$$\frac{\partial \rho \phi}{\partial t} + \nabla(\rho \vec{v} \phi) = \nabla \cdot (\Gamma_\phi \nabla \phi) + S_\phi \tag{3}$$

where the scalar quantity ϕ, the diffusion coefficient Γ_ϕ and the source term S_ϕ are presented in Table 2. This includes turbulent kinetic energy (k) and the dissipation rate (ε) for the low-Reynolds-number k-ε turbulence model.

As illustrated in Fig. 1, the free air domain is represented as a cuboid. The bottom boundary consists of an adiabatic concrete ground, while a water surface is located at its midpoint. No-slip conditions are imposed on the ground surface, the water surface, and all faces of the PV module. The bottom boundary comprises two distinct regions. The water surface is modeled as an aerodynamically smooth wall, where the viscous sublayer is directly resolved to accurately capture near-wall flow physics. Conversely, the ground is treated using a wall-function approach, and a sand-grain roughness height of 3.5 μm is used. Among the remaining five boundaries, one serves as the air inlet, while the other four are treated as open boundaries. In contrast to a conventional outlet boundary, open boundaries allow air to enter and exit the domain in response to the local pressure field, ensuring a more realistic depiction of unconfined natural environments. The mathematical formulations for the boundary conditions are provided in Table 3.

In this study, a typical medium turbulence intensity I_T of 5% is adopted, corresponding to common engineering scenarios such as ventilation or general external flows. This value serves as a reasonable engineering approximation; it avoids numerical instabilities often associated with unrealistically low turbulence levels while not overestimating turbulent diffusion. Furthermore, due to the heterogeneous surface roughness (transition from ground to water) and the low-altitude configuration of the PV module, a defined freestream velocity is applied at the inlet boundary, and the boundary layer is allowed to develop spatially within the domain. The near-surface velocity gradient is thus resolved through the characteristics of the boundary layer and the no-slip conditions at the ground and water surfaces. In the absence of a PV module, the resolved velocity profile over the water surface approximates Eq. (4), using the boundary layer height as the reference height h_r. These boundary condition settings have been justified in previous studies on natural water bodies [46].

$$u = u_a \left(\frac{h}{h_r} \right)^{0.11} \tag{4}$$

The numerical solver employs finite element discretizations of the steady-state RANS equations, using a segregated approach that updates turbulence and flow variables sequentially during each nonlinear iteration. This decoupled strategy facilitates efficient computation through a preconditioned Generalized Minimal Residual (GMRES) algorithm, which is particularly well-suited for solving large, sparse, and asymmetric equation systems with low memory requirements. All simulations

Table 2
Summary of governing equations.

Equation	ϕ	Γ_ϕ	S_ϕ
Continuity	1	0	0
x-Momentum	U	$\mu+\mu_t$	$-\frac{\partial p}{\partial x}+F_x$
y-Momentum	V	$\mu+\mu_t$	$-\frac{\partial p}{\partial y}+F_y$
z-Momentum	W	$\mu+\mu_t$	$-\frac{\partial p}{\partial z}+F_z$
k	k	$\mu+\frac{\mu_t}{\delta_k}$	$P_k-\rho\varepsilon$
ε	ε	$\mu+\frac{\mu_t}{\delta_\varepsilon}$	$C_{\varepsilon 1}\frac{\varepsilon}{k}P_k-f_\varepsilon C_{\varepsilon 2}\rho\frac{\varepsilon^2}{k}$
where			
$C_{\varepsilon 1}=1.44, C_{\varepsilon 2}=1.92, \delta_k=1.0, \delta_\varepsilon=1.44$			
$P_k=\mu_t(\nabla u:(\nabla u+(\nabla u)^T)-\frac{2}{3}(\nabla\cdot u)^2)-\frac{2}{3}\rho k\nabla\cdot u, \mu_t=\rho C_\mu\frac{k^2}{\varepsilon}f_\mu$			

μ: dynamic viscosity, μ_t: turbulent viscosity, F: external body force,
P_k: the production term, f_μ, f_ε: damping functions
$C_{\varepsilon 1}, C_{\varepsilon 2}, \delta_k, \delta_\varepsilon$: turbulence model constant parameters.

Table 3
The boundary conditions.

Type of boundary	k	ε
Velocity inlet	$3/2(U_T I_T)^2$	$C_\mu^{3/4}k^{3/2}/L_T$
Open boundary	$3/2(U_{\text{ref}} I_T)^2$	$C_\mu^{3/4}k^{3/2}/L_T$
Water surface	0	$\lim_{\ell_w\to 0} 2\upsilon k/\ell_w^2$
Ground surface	0	$\frac{C_\mu^{3/4}k^{3/2}}{\kappa\delta_w}$

I_T: turbulence intensity, L_T: turbulence length scale, ℓ_w: wall distance variable
C_μ: turbulence model constant parameter, U_T: inlet velocity, U_{ref}: reference velocity scale
κ: von Kármán constant, δ_w: wall lift-off distance.

are conducted on a Windows Server (x64) system powered by an AMD Ryzen Threadripper 3970X (32-core processor) with 128 GB of RAM. Prior to analyzing the results, a grid convergence test and validation of the numerical model are performed, as detailed in Appendices B and C.

3. Results and discussion

Using the established 3-D numerical model, detailed wind fields for various PV module placements are analyzed. Subsequently, the effects of variations in u_a, h, β, and θ on the wind speed over the water surface are systematically examined. The underlying mechanisms are analyzed, and the relative wind speed u_r is evaluated as a key indicator of under-panel ventilation performance. Finally, a generalized correlation for u_r is derived to quantify these effects.

3.1. PV-induced flow patterns and the underlying mechanisms

To clearly elucidate airflow beneath the PV panel, PV-induced flow patterns for various configurations under south and north winds are analyzed. In general, at the same inlet wind speed, northerly and southerly winds generate comparable flow disturbances around the module but induce opposite effects on the near-water wind speed. The numerical simulation results are further examined to extract deeper insights into these contrasting behaviors.

3.1.1. Under south and southeast wind conditions

Under southerly wind conditions, the streamlines around a module installed at a height of 1 m are analyzed for varying tilt angles β, as shown in Fig. 3. The airflow moves from left to right, interacting with the ground surface, water surface, and the module.

The obstruction caused by the PV module creates a downstream deceleration zone in the free-stream airflow. When β exceeds 20°, flow separation occurs, initiating vortex formation, which evolves into two distinct cells as β exceeds 60°. However, the airflow near the water surface remains largely unaffected by the deceleration zone, while the wind speed increases significantly with increasing β. This phenomenon is primarily attributed to the formation of a channel between the low-velocity wake and the water surface, where the wind speed is inversely correlated with the cross-sectional area. As β increases, the windward projection of the module expands, narrowing the passage and accelerating the airflow. Consequently, at a fixed h, the near-water wind speed is expected to follow a sinusoidal trend with β.

As the distance between the PV module and the water surface increases, the channeling effect diminishes rapidly. As a result, the airflow over the water becomes predominantly influenced by the boundary layer, closely approximating conditions without the PV module. Fig. 4 illustrates the flow fields for varying h with $\beta = 60°$ and $\theta = 135°$ (southeast winds). When h reaches 1.5 m or higher, the module exerts minimal influence on wind speeds near the water surface, underscoring that h defines the spatial reach of its aerodynamic influence.

Furthermore, compared to south winds when $h = 1$ m, the obstructive area of the PV module to airflow is reduced under southeast winds, leading to the formation of vortices on its leeward side. Consequently, the low-velocity wake region is smaller at $\beta = 60°$, and the flow acceleration beneath the panel is weaker than that observed under south winds.

Physically, the flow characteristics around the PV module under south and southeast wind conditions are governed by two distinct aerodynamic mechanisms: the wake shielding effect behind the panel and the flow acceleration effect beneath it. In the wake region, a pronounced low-velocity zone begins to form behind the panel once the tilt angle reaches 20°. From a fluid dynamics perspective, the aerodynamic drag force on the panels is directly proportional to their frontal projected area relative to the wind direction. As the tilt angle increases, the larger windward projection significantly amplifies wind resistance, thereby intensifying the momentum deficit in the wake. Notably, provided there is sufficient clearance from the water surface, the development of this wake structure remains largely independent of the installation height. Conversely, the flow dynamics beneath the panel exhibit an opposing trend. The gap between the PV module and the water surface creates a constricted channel for airflow. According to the principle of mass conservation (continuity equation), the airflow obstructed by the panel frontal area is diverted through this clearance. To maintain a mass flow rate consistent with the upstream flow, the fluid accelerates as it passes through the narrowed area. As a result, a lower installation height creates a tighter channel, significantly amplifying this channeling effect and producing higher local wind speeds near the water surface.

3.1.2. Under north and northeast wind conditions

Under northerly wind conditions, the airflow moves from right to left, as illustrated in Fig. 5. While similar flow acceleration occurs beneath the PV module, it originates at the lower edge of the module, affecting less than half of the water surface. Consequently, the average acceleration over the water surface is significantly smaller compared to southerly winds, which influence more than half of the water surface area. On the other hand, the module obstructs the airflow, causing air to converge around its edges. The resulting convergence raises the local

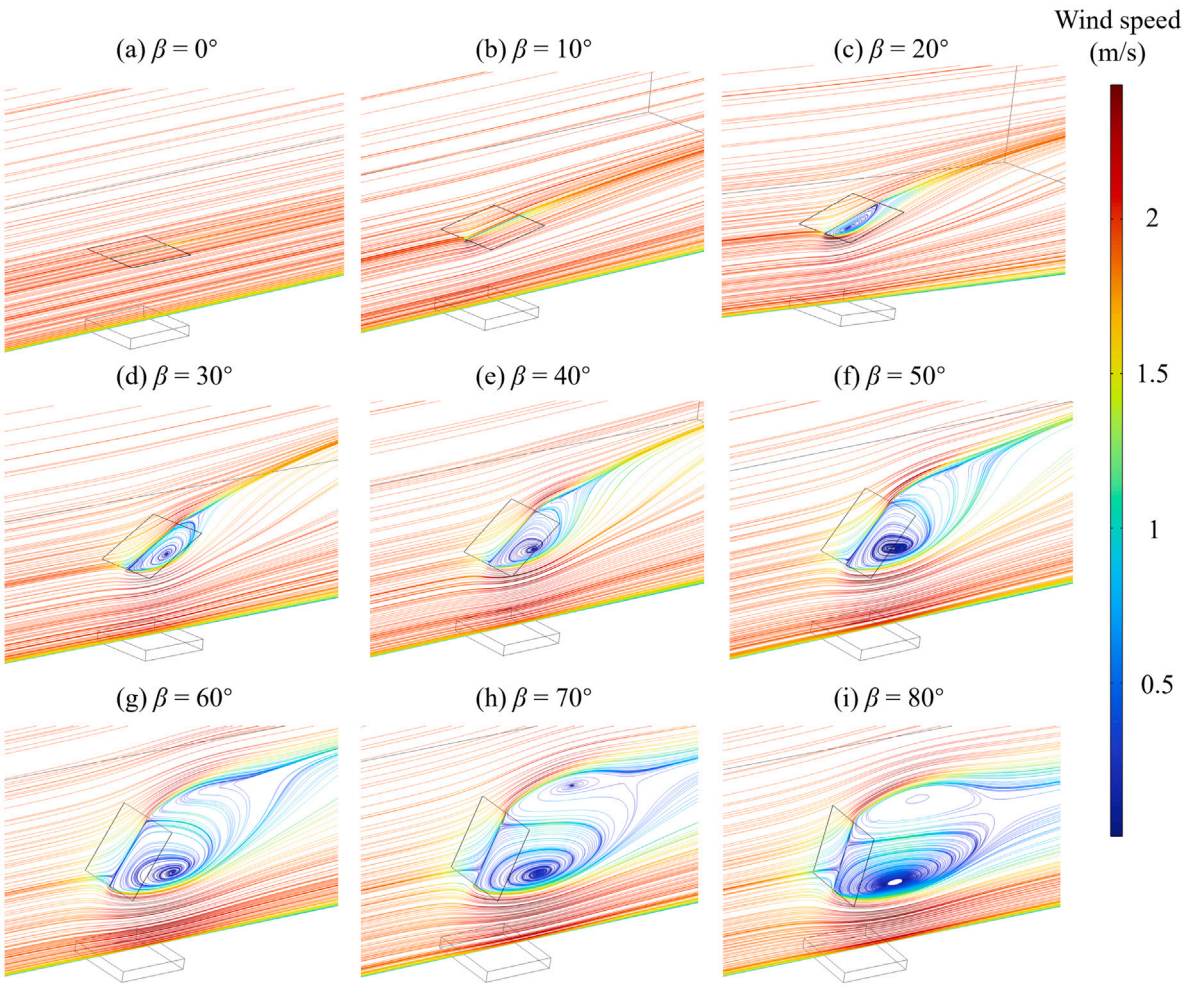

Fig. 3. Wind velocity fields around the PV module when installation height h = 1 m under 2 m/s south wind, for tilt angles β of (a) 0°, (b) 10°, (c) 20°, (d) 30°, (e) 40°, (f) 50°, (g) 60°, (h) 70°, (i) 80°.

pressure and generates an adverse pressure gradient, which slows down the wind over the water surface. Since this deceleration is an indirect effect, it results in milder velocity changes over the water surface.

Therefore, the wind velocity over the water surface results from a trade-off between channel-induced acceleration and obstruction-related deceleration, with the latter prevailing in most cases under northerly winds. When β exceeds 20°, the accelerated flow at the entrance of the channel begins to influence the water area, while the deceleration effect simultaneously intensifies. The interaction between these two mechanisms generates oscillations in wind speed over the water surface, with the dominant effect determined by their respective influence ranges and intensities over the water surface.

The airflow patterns also exhibit a strong dependence on the installation height of the PV modules. Fig. 6 reveals that the deceleration effects under northeast winds are less pronounced than those under north winds. At h above 1 m, the obstruction zone does not reach the water surface, allowing channel-induced acceleration to dominate. As a result, the streamlines near the water surface indicate a slight increase in wind speed under elevated configurations; however, this effect is no longer observable when h exceeds 1.5 m.

In summary, the downstream flow field under north and northeast winds closely resembles that observed under south winds; it is primarily governed by the windward projected area and demonstrates only a weak dependence on installation height. However, the acceleration channel beneath the panel mainly develops after the airflow has passed over the water surface, exerting minimal impact on near-surface airflow. Instead, elevated local pressure decreases wind velocity near the water, which explains why greater aerodynamic resistance from the module results in lower surface wind speeds.

3.2. Effects of ambient wind speed

The development of local airflow fields within the aquavoltaic system is influenced by both environmental conditions (e.g., wind speed and direction) and PV installation configurations (e.g., height and tilt angle). To quantify the effects of the PV module on near-water wind speed under varying environmental and configuration conditions, we further examine how the relative wind speed (as defined in Eq. (2)) changes with these parameters. Since the wind speed, u_a, influences both u_{PV} and u_{natural} in Eq. (2), a detailed quantitative analysis is conducted to determine the dependence of u_r on u_a as a first step.

Three different wind speeds, 1 m/s, 2 m/s, and 4 m/s, are compared, with u_a = 2 m/s serving as the baseline. The differences in u_r relative to the baseline case for various panel heights, tilt angles, and wind directions are presented in Fig. 7. Positive values indicate that u_r is higher than the baseline, while negative values signify the opposite.

The results indicate that the influence of inlet wind speed u_a on relative wind speed u_r is primarily governed by wind direction. For southerly winds, smaller h and larger β induce stronger flow disturbances, amplifying the differences in u_r. Conversely, under northerly winds, u_r is relatively insensitive to h and β, exhibiting only minor variations across different configurations. Moreover, direct comparisons reveal that higher u_a counterintuitively reduce u_r over the water surface. This phenomenon arises because stronger winds amplify turbulent

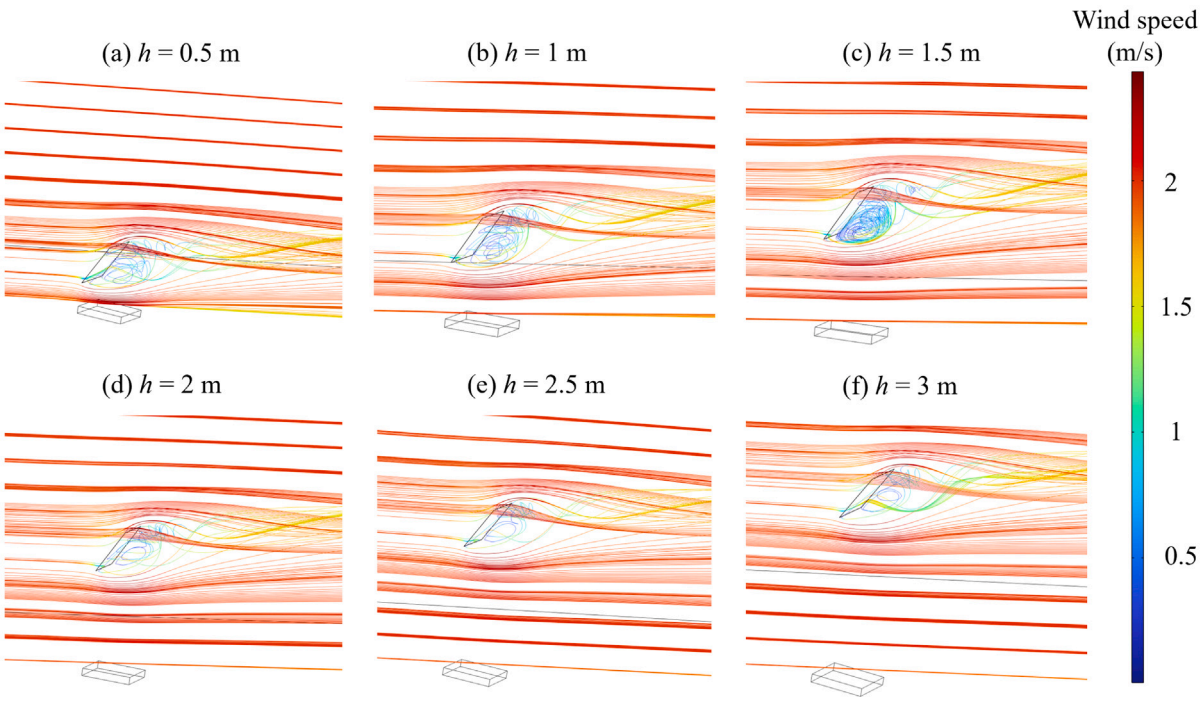

Fig. 4. Wind velocity fields around the 60° tilted PV module under 2 m/s southeast wind, at PV height h = (a) 0.5 m, (b) 1 m, (c) 1.5 m, (d) 2 m, (e) 2.5 m, (f) 3 m.

mixing, thereby increasing frictional resistance and viscous dissipation, which leads to greater energy losses in the flow. Consequently, the channeling acceleration effect beneath the panels is more pronounced under lower wind speed conditions.

In all cases, different u_a across the four representative wind directions result in less than a 1% change in u_r. This indicates that the velocity within the boundary layer is largely proportional to the ambient flow velocities, leading to negligible variations in u_r. Therefore, the following section focuses on the effects of wind direction and PV configurations on u_r, while maintaining a constant wind speed of u_a = 2 m/s.

3.3. Effects of PV configurations and wind directions

As illustrated in Section 3.1, the PV module acts as an aerodynamic barrier, causing significant flow deceleration in its wake. However, the airflow velocity beneath the module results from complex interactions involving boundary layer flow, edge flow, and turbulent separation vortices. These flow dynamics exhibit non-linear variations influenced by PV configurations and wind direction θ, which can be quantitatively assessed using relative wind speed u_r as an indicator of airflow modification, as presented in Fig. 8.

For southerly winds, when θ aligns with the PV module's azimuth angle, airflow directly impinges on its upper surface. At β = 0°, the module has negligible impact on wind speed over the water, resulting in u_r = 1.0 irrespective of h. As the tilt angle increases, airflow acceleration near the water surface becomes evident. When h > 1.5 m, u_r demonstrates an approximately linear relationship with β, with the slope decreasing as h increases. For h = 0.5 m, u_r shows exponential growth as β increases from 0° to 20°, logarithmic growth from 20° to 60°, and minimal variation beyond 60°, peaking at 1.25 for β = 80°. A similar pattern is observed at h = 1 m/s, where u_r increases linearly with β up to 60°.

Under southeasterly winds, the acceleration effects are similar to those seen in southerly winds but are weaker overall. The trend remains consistent across different h: u_r increases linearly with β up to 50° and then remains nearly constant. The differences between 70° and 80° are negligible, with the peak wind speed enhancement stabilizing at a maximum value of 18% (u_r = 1.18).

For winds from the north and northeast, aerodynamic responses to tilt angle β and panel height h are opposite to those observed in southerly winds, resulting in wind speed deceleration over the water surface. Additionally, the relationship between u_r and β becomes non-monotonic, particularly when β is between 20° and 40°, as shown in Fig. 9. At small β, near-water flow is dominated by a low-velocity zone generated by the sheltering effect beneath the PV module. As β increases, the channeling effect accelerates the wind speed over the water surface, while the expanding deceleration zone imposes an opposing impact. These competing mechanisms jointly control u_r. Overall, deceleration predominates in most configurations, especially at lower tilt angles. When h > 1.5 m, u_r initially decreases before increasing with β, reaching a minimum at β = 20° under north winds and β = 30° under northeast winds. For h = 1 m, u_r under northeast winds follows a similar trend, whereas u_r under north winds gradually decreases with β up to 40° and stabilizes beyond 60°. The maximum deceleration occurs when h = 0.5 m under north winds: after a slight increase at β = 30°, u_r decreases with β, with the gradient diminishing beyond 60°, ultimately reaching a 15% reduction (u_r = 0.85) at β = 80°.

Under easterly winds, airflow crosses the PV module laterally, exerting minimal influence on the flow field over the water surface. Variations of u_r with β are minimal, with deviations smaller than 0.2%, indicating negligible effects.

Variations in u_r under different wind directions align with the principles of the windward projected area and local pressure gradients discussed in Section 3.1. The quantitative results provide a clearer and more precise assessment of the specific impacts of different PV configurations. Interestingly, the analysis reveals that h determines the upper limit of u_r variation; once the module is elevated beyond a certain distance from the water surface, changes in β have little effect on the near-water wind field.

The relationship between u_r and h for different β values is depicted in Fig. 10. The results reveal that, although southerly and northerly winds produce opposing changes in wind speed near the water surface, both exhibit similar u_r variations with respect to panel height, following

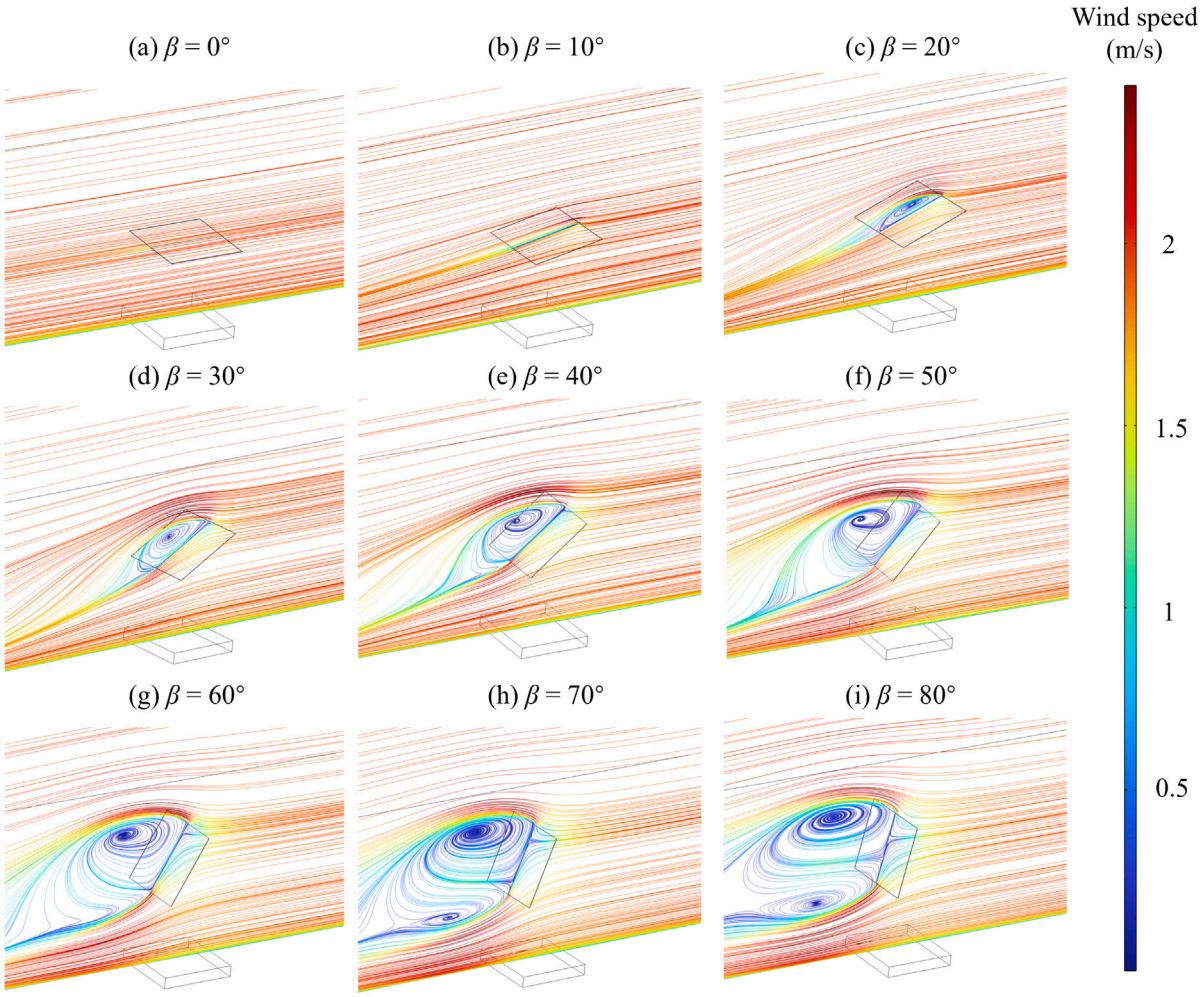

Fig. 5. Wind velocity fields around the PV module when installation height h = 1 m under 2 m/s north wind, for tilt angles β of (a) 0°, (b) 10°, (c) 20°, (d) 30°, (e) 40°, (f) 50°, (g) 60°, (h) 70°, (i) 80°.

an exponential trend when $h < 1.5$ m. For $h > 1.5$ m, u_r values remain between 0.97 and 1.03, indicating less than 3% change in near-water wind speed when PV modules are placed.

3.4. Generalized expression for the relative wind speed

The preceding discussions have identified three key factors that affect u_r, i.e. panel height h, tilt angle β, and wind direction θ. Comprehensive simulations reveal a consistent relationship between u_r and these parameters, particularly under southerly winds. This observation suggests the feasibility of developing a generalized mathematical expression to easily estimate u_r under varying outdoor conditions without the need for CFD simulations.

Within the atmospheric boundary layer, the variation of wind speed with height is typically described using a power law profile, where the exponent depends on surface roughness and atmospheric stability in the vertical direction. However, obstacles such as PV modules disturb incoming airflow, creating a composite field that blends the undisturbed free stream with perturbed flows. Theoretically, the airflow acceleration or deceleration can be assumed to begin at the lower edge of the PV module, so the velocity profile from that point to the water surface can still be approximated by the power law. For the disturbed flow, the equivalent wind speed could be estimated by integrating potential flow theory with the standard power law, and an expression for u_r is proposed:

$$u_r = \sqrt{1 + 2w\cos\beta'} \cdot \left(\frac{h + L\sin\beta}{h}\right)^{\alpha} \tag{5}$$

where w represents the ratio of the surface normal perturbation velocity to u_a, and α is the power-law exponent that determines the gradient of u_r with respect to h. β' is the angle of incidence of the wind on the PV module, which facilitates the trigonometric decomposition of the velocity components on the PV surface. The detailed derivation of this expression is presented in Appendix A.

The determination of w and α is complicated by the interaction of multiple flow patterns. The coefficient values in the proposed formula are obtained by fitting simulation data under different wind directions. As shown in Fig. 11, the formula agrees excellently with the numerical results for south and southeast winds, deviating by less than 2%. For north and northeast winds, although the semi-empirical formula cannot fully capture subtle tilt angle-dependent fluctuations arising from flow instability, it accurately reproduces the overall trend with maximum errors below 4%.

To further elucidate how the two fitted coefficients w and α vary as a function of the wind direction angle θ, additional simulations for θ = 112.5° are included. This expanded dataset yields five sets of fitted coefficients, as summarized in Table 4.

The fitted coefficients vary systematically with wind direction, displaying notable differences between south and north winds. As illustrated in Fig. 12(a), the perturbation velocity ratio w displays three distinct linear regimes corresponding to θ: northerly (0°-90°), southeasterly (90°-135°), and southerly (135°-180°) winds, each characterized by a unique slope. Additionally, as shown in Fig. 12(b), it is observed that for southerly winds, the coefficient α is proportional to

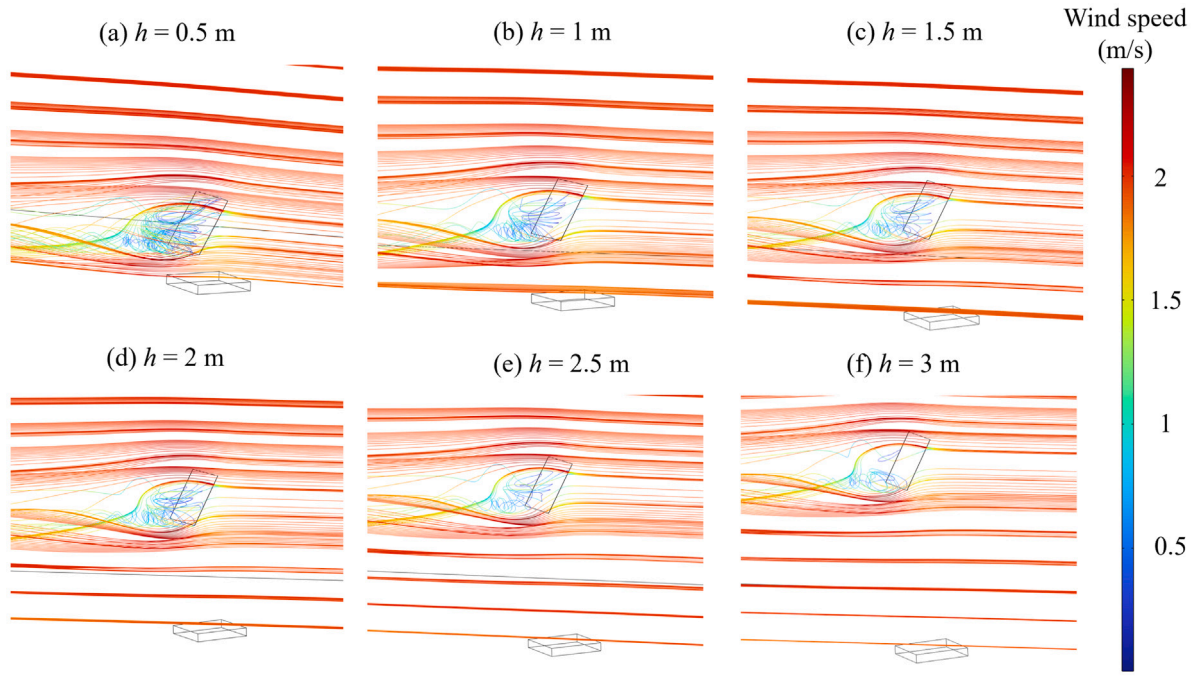

Fig. 6. Wind velocity fields around PV module with 60° tilt angle under 2 m/s northeast wind, at PV height h = (a) 0.5 m, (b) 1 m, (c) 1.5 m, (d) 2 m, (e) 2.5 m, (f) 3 m.

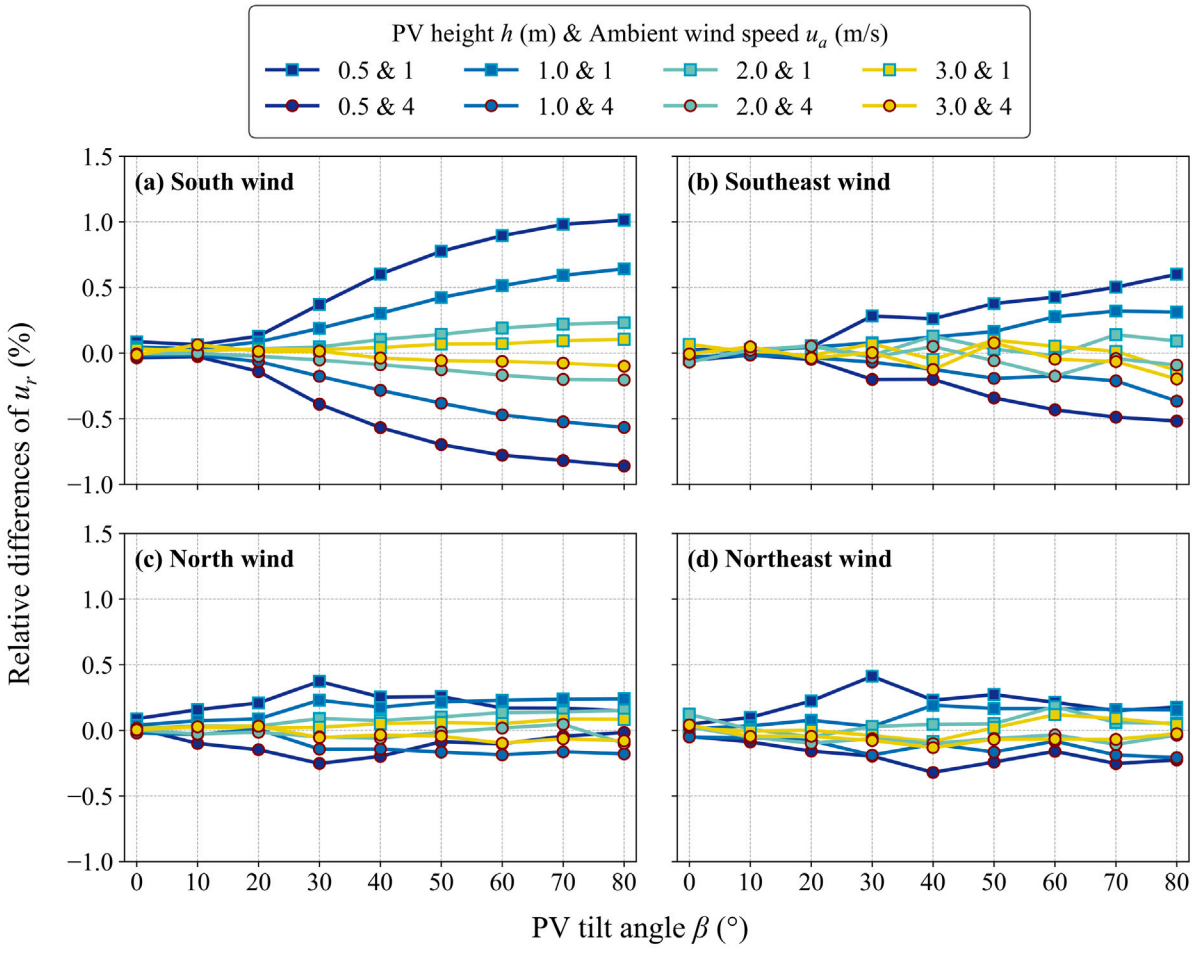

Fig. 7. The relative difference in u_r for u_a = 1 m/s (indicated by cyan marker borders) and u_a = 4 m/s (indicated by red marker borders), compared to the baseline case of u_a = 2 m/s, for varying panel heights (h), tilt angles (β), and wind directions (θ).

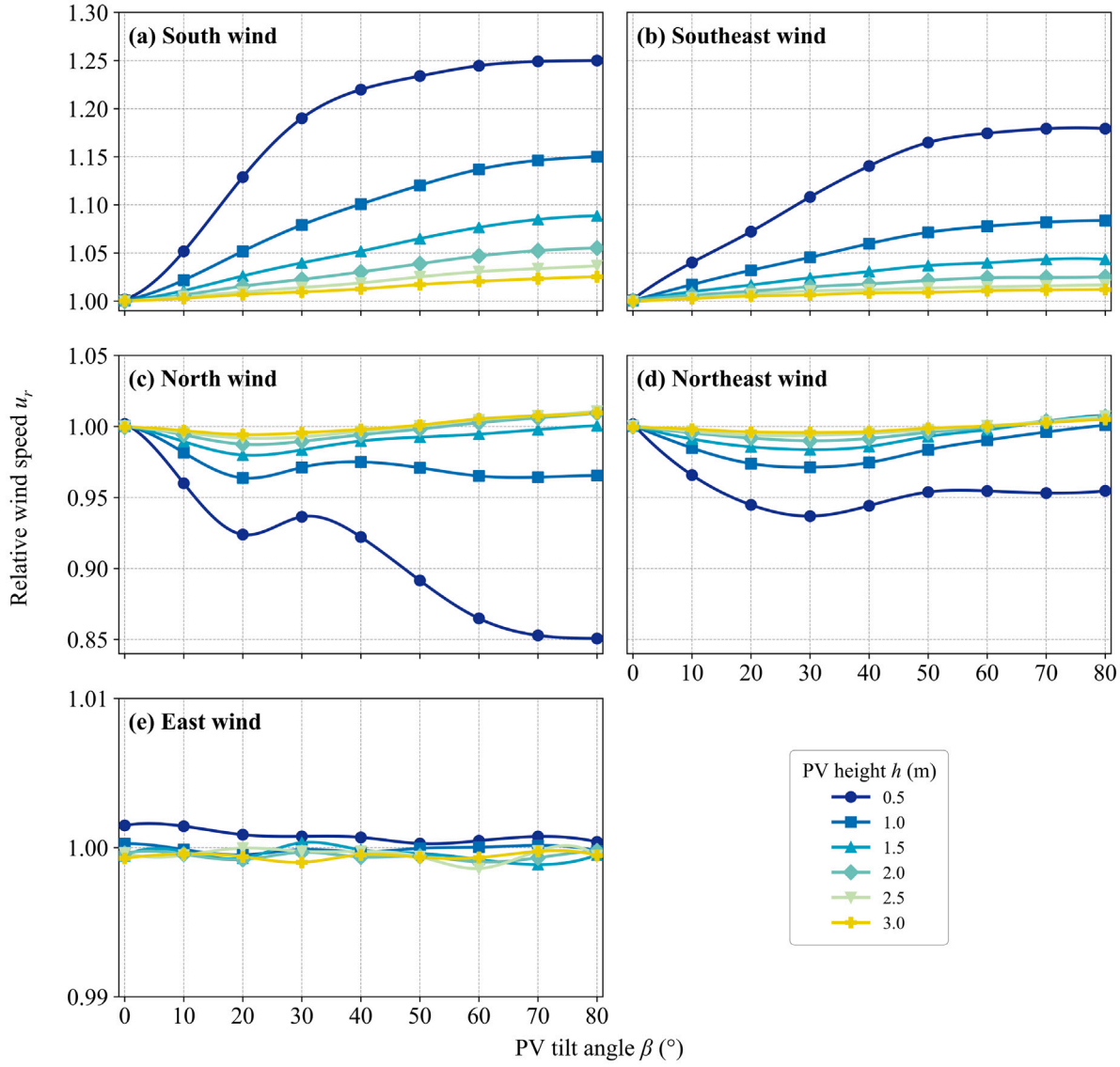

Fig. 8. The relative velocity u_r with respect to PV tilt angle β and installation height h, under different wind directions: (a) south wind; (b) southeast wind; (c) north wind; (d) northeast wind; and (e) east wind.

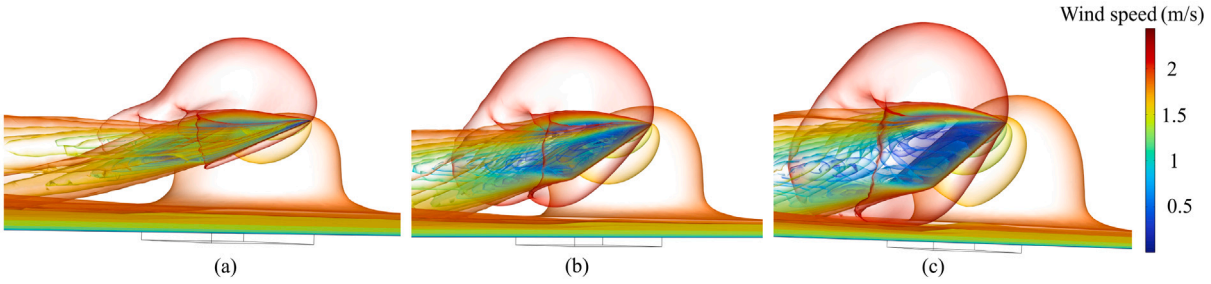

Fig. 9. 3-D flow field isosurfaces around the PV module when installation height h = 0.5 m under north winds, for tilt angle β of (a) 20°; (b) 30°; (c) 40°.

the cosine of θ, whereas for northerly winds, it is directly proportional to θ:

For southerly winds with $\theta > 90°$: $\alpha(\theta) = \alpha(180°)\cos(180° - \theta)$

For northerly winds with $\theta < 90°$: $\alpha(\theta) = 0.0022\theta - 0.18$

To further validate the generalizability of the proposed formula, we applied it to data with a wind direction of θ = 157.5°, where w was determined by linear interpolation and α was calculated by substitution into the cosine relationship (i.e., w = 0.06775 and α = 0.25). As illustrated in Fig. 13, the formula accurately captures the numerical simulation results, achieving an average error of just 0.56% across all

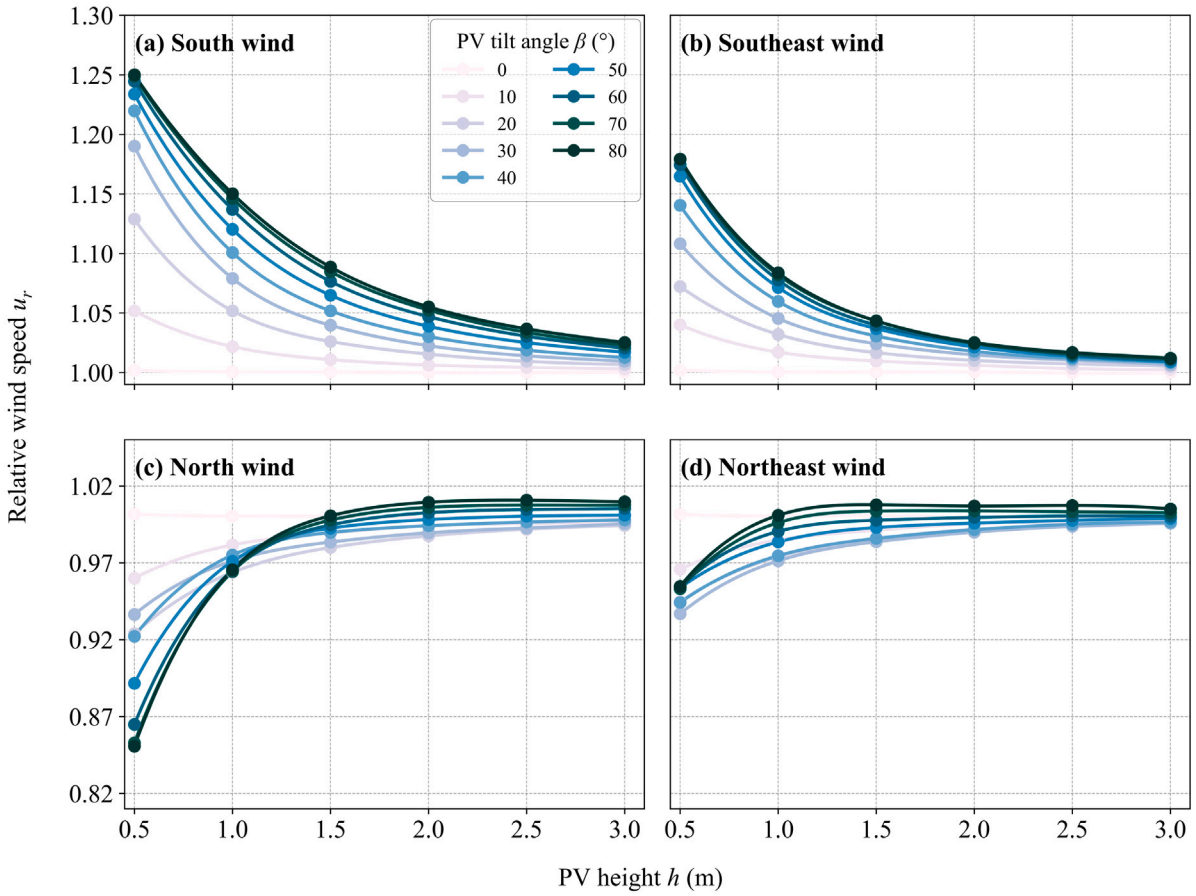

Fig. 10. The relative velocity u_r with respect to PV installation height h and tilt angle β, under different wind directions: (a) south wind; (b) southeast wind; (c) north wind; (d) northeast wind.

Table 4
Fitting coefficients of w and α for different wind direction angles θ.

θ (°)	w	α
0	0.076	−0.180
45	0.046	−0.079
112.5	0.037	0.0722
135	0.070	0.195
180	0.055	0.269

test cases. This demonstrates the broader applicability and robustness of the proposed formula.

3.5. Practical implications

Beyond characterizing the near-water wind field, the observed relationship between u_r and h provides valuable insights into ventilation beneath the PV module, which is critical for module cooling and overall system efficiency. Specifically, as u_r approaches 1, it indicates a decoupling of the aerodynamic interaction between the PV module and the water surface. In this regime, the module exerts negligible disruption on the near-water flow, while the water surface imposes minimal obstruction to the development of under-panel airflow. This state corresponds to unimpeded ventilation, suggesting that the channeling effect is not an intrinsic feature but rather a conditional phenomenon dependent on h and β. Accordingly, fluctuations in u_r indicate that the water surface obstructs airflow beneath the panel, thereby reducing ventilation efficiency.

Based on these findings, this study assumes that variations in wind speed above the water surface within 5% represent normal ventilation within the PV-water clearance. It can be concluded that, under southerly winds, installing PV modules at a height of 2 m or more above the water surface ensures adequate ventilation and cooling performance, regardless of the tilt angle. For southeasterly winds, this threshold is reduced to 1.5 m, while under northerly and northeasterly winds, a clearance of just over 1 m is sufficient to maintain effective ventilation.

On the other hand, microclimatic variations induced by u_r can be evaluated using established theoretical models. In particular, water evaporation is quantified via the Penman–Monteith equation, a widely recognized standard for evapotranspiration that has been successfully adapted to open-water contexts, including FPV systems [47]. It exhibits robust performance across diverse climatic zones.

$$E = \frac{0.408\,\Delta\,(Q^* - G) + \gamma\,\dfrac{900}{T+273}\,u\,(e_s - e_a)}{\Delta + \gamma\,(1 + 0.34\,u)} \tag{6}$$

where T and u are the ambient air temperature and velocity, respectively. Δ represents the slope of the saturation vapor pressure–temperature relationship at mean air temperature and γ is the psychrometric constant (0.066 kPa/°C), $(Q^* - G)$ represents the net available energy at the surface, defined as the difference between the net radiation (Q^*) and the surface heat flux (G), (e_s-e_a) represents the vapor pressure deficit (VPD) of air.

To quantify the potential changes in evaporation rates, we performed an estimation under representative environmental conditions. The parameters are selected to reflect a typical temperate or subtropical climate during a clear summer day, characterized by moderate heat

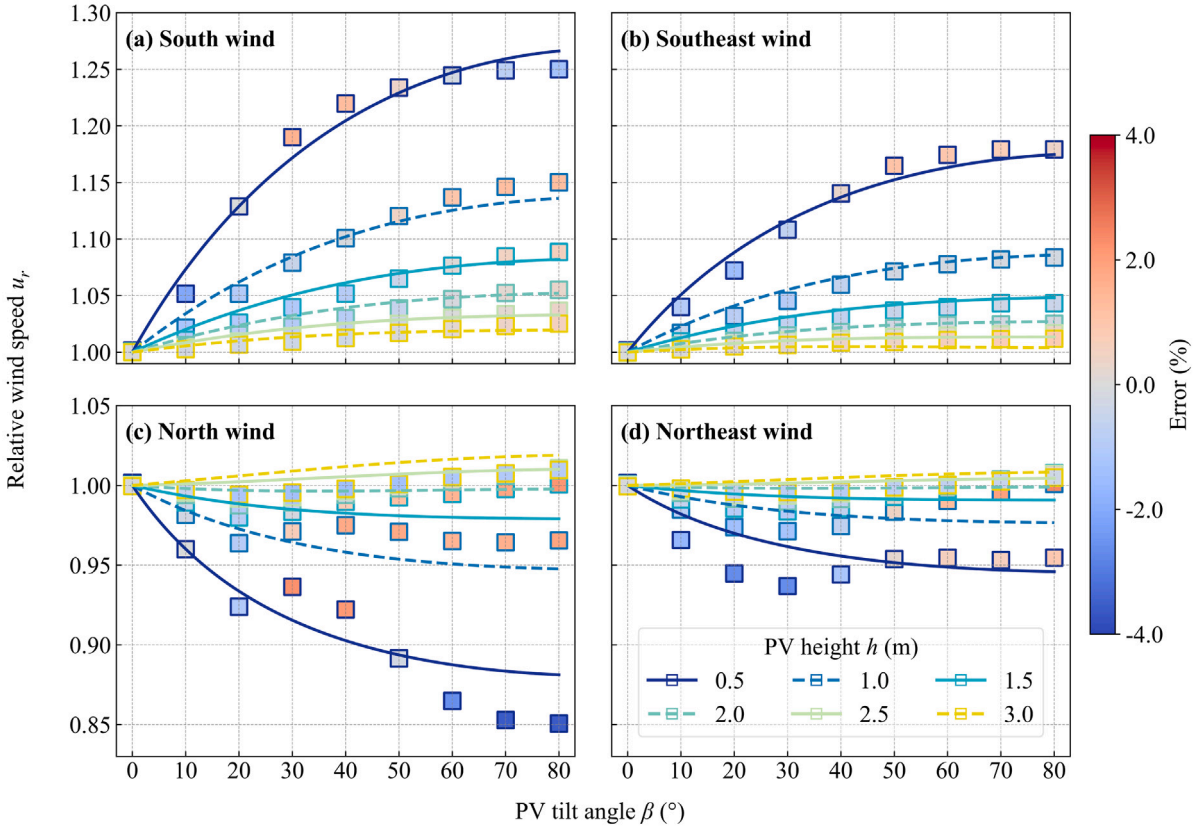

Fig. 11. Comparison of the semi-empirical formula (lines) and simulation results (markers) for different wind direction: (a) south wind; (b) southeast wind; (c) north wind; (d) northeast wind.

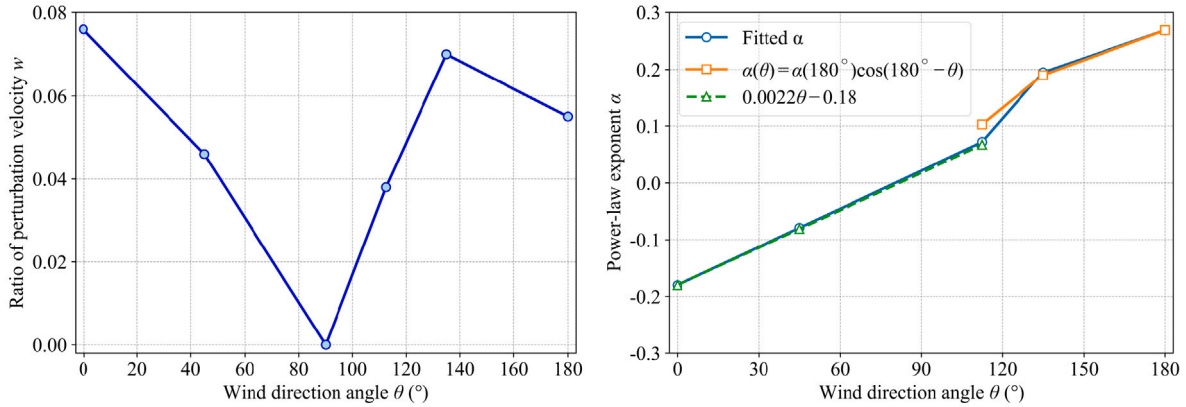

Fig. 12. Variation of fitting coefficients with θ, (a) ratio of perturbation velocity w; (b) power-law exponent α and its relationship with the cosine of deviation angle.

and humidity. Specifically, T is set to 25 °C with a relative humidity of 0.5, and $Q^* - G$ is assumed to be 15 MJ/m^2/day. For the baseline calculation, a reference velocity of 1.81 m/s is employed. This value represents the average wind speed within the boundary layer above the water surface, derived from simulations with a 2 m/s inlet velocity without a PV module.

Based on the calculations from Eq. (6), the natural water evaporation rate (E) without PV module is 6.14 mm/day. When the PV panel is installed at a height of 0.5 m and considering only the effect of wind speed, the maximum reduction in surface wind speed is 15% under northerly winds, resulting in a decrease of 0.22 mm/day in the evaporation rate. Conversely, under southerly winds, the wind speed increases by up to 25%, raising the evaporation rate by 0.33 mm/day. Overall, u_r variations result in evaporation rate fluctuations ranging from −3.6% to +5.4%.

Furthermore, wind speed over the water surface plays a decisive role in the convective heat exchange between the water body and the atmosphere, affecting turbulent mixing at the air–water interface and, consequently, altering water temperature. This effect can be assessed by establishing the relationship between wind speed and the convective heat transfer coefficient (h_c). The Nusselt number (Nu) serves as the

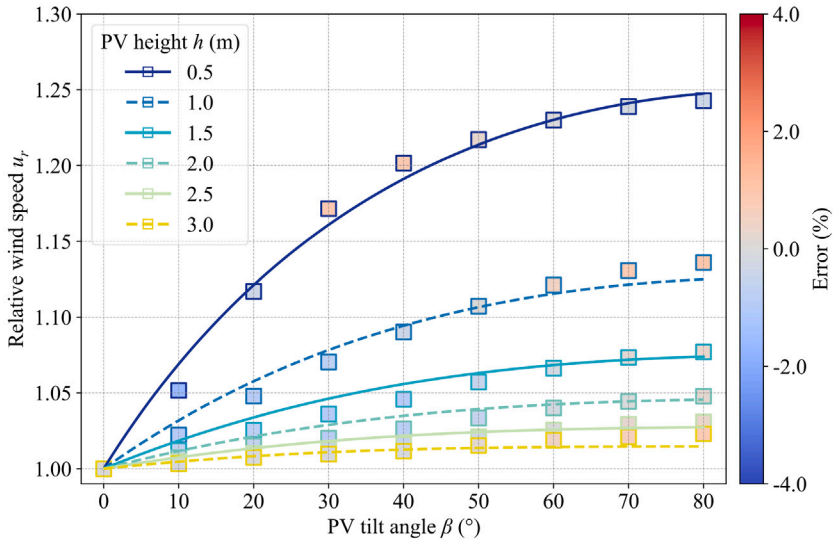

Fig. 13. Comparison of simulated (markers) and formula-estimated (lines) results under a wind direction θ = 157.5°, with the estimated w obtained through linear interpolation and α derived using the cosine relationship.

dimensionless expression of h_c. By invoking the Chilton–Colburn analogy, the local Nu for turbulent flow is derived from the local friction coefficient, yielding the classical correlation for external flow [48], as presented in Eq. (7).

$$\mathrm{Nu} = \frac{h_c l_c}{k} \approx 0.0296 \mathrm{Re}_l^{4/5} \mathrm{Pr}^{1/3} \tag{7}$$

Under the given environmental conditions, the typical physical properties of standard dry air at 25 °C are adopted, yielding a Prandtl number (Pr) of 0.724, which falls within the validity range (0.6–60) of the applied correlation. The characteristic length is defined as the distance from the air inlet to the water surface within the model. In the baseline condition without the PV module, h_c is calculated to be 5.073 W/(m^2·K). Subsequently, the impact of PV-induced wind speed variations is evaluated: a 25% increase in wind speed raised h_c by 0.991 W/(m^2·K), while a 15% decrease reduced it by 0.619 W/(m^2·K). Consequently, the variations in wind speed over the water surface induced by the PV modules lead to a fluctuation in the convective heat transfer coefficient ranging from −12.2% to +19.5%.

In summary, u_r serves not only as a metric for evaluating ventilation performance beneath the panel but also as a proxy for assessing the microclimate above the water surface. This establishes a unified framework for aquavoltaic design that simultaneously optimizes heat dissipation performance and environmental compatibility.

4. Conclusions

This study establishes a 3-D numerical model to analyze the wind field around the PV module in a standalone aquavoltaic system across 738 cases, employing the proposed relative wind speed (u_r) over water to assess its impacts on panel ventilation and the aquatic microclimate. The investigation systematically evaluates the diverse flow patterns induced by module tilt angle (β), height (h), and wind direction (θ), and quantifies the corresponding u_r, whereas the influence of ambient wind speed (u_a) is found to be negligible. Based on the observations and analysis of the simulation results, the following conclusions can be drawn:

The south-facing PV module accelerates water surface airflow by generating a channeling effect under southerly winds. Conversely, under northerly winds, a competing interaction arises between the channeling-induced acceleration and the deceleration caused by adverse pressure gradients, typically resulting in a reduction of u_r. Notably, the dominance of these mechanisms is strongly influenced by the mounting height, suggesting that the PV does not always impede airflow over the water surface. Specifically, the quantified results for u_r show that when β exceeds 50°, further increases produce only marginal variations. Flow disturbances increase with rising β and decreasing h, peaking at h = 0.5 m and β = 80°, where u_r rises to 1.25 under south winds and decreases to 0.85 under north winds. Under northerly winds, u_r exhibits non-monotonic behavior between β = 20° and 40°. Under east–west winds or at β = 0°, the module produces negligible aerodynamic blockage, leaving the flow field over the water surface virtually undisturbed. Across all wind directions, when h exceeds 1.5 m, variations in wind speed within the velocity boundary layer become minimal.

In addition to providing physical insights, this work introduces an analytical framework for evaluating u_r without relying on numerical simulations. By incorporating the equivalent wind speed into the power-law expression, a semi-empirical formula for u_r is derived through regression analysis. Using fitted coefficients for the perturbation velocity ratio and the power-law exponent, the deviation between the formula estimates and the numerically calculated u_r is less than 4%. Moreover, we found that these coefficients exhibit segmented trends concerning the wind direction angle θ: the power-law exponent is proportional to the cosine of θ under southerly winds and to θ under northerly winds. This formulation can be generalized to a broader range of wind directions, and its validity has been verified through case studies.

Building on these results, a threshold is proposed for identifying adequate ventilation, and correlations of u_r with both the evaporation rate and the convective heat transfer coefficient under typical meteorological conditions are established, extending the theoretical results to practical applications. The analysis reveals that the required clearance height of the PV module above the water surface to ensure effective ventilation varies with wind direction: at least 2 m for southerly winds, 1.5 m for southeasterly winds, and just over 1 m for northerly and northeasterly winds. In addition, under the same environmental conditions, the identified variations in u_r lead to changes in the evaporation rate ranging from −3.6% to +5.4%, and in the convective heat transfer coefficient ranging from −12.2% to +19.5%. Therefore, u_r can serve as a valuable indicator for evaluating the heat dissipation performance of the PV module and water surface, thus facilitating environmentally sustainable design and the optimal deployment of aquavoltaic systems.

However, this study has limitations that require continued investigation. For instance, a key simplification in this study is the representation of the water surface as a flat, stationary boundary with a

no-slip condition. This approach, common in many numerical studies of near-surface airflow, offers computational tractability and is physically representative of perfectly calm water conditions. However, it does not account for the dynamic modifications induced by surface waves, which arise under even moderate wind forcing. Experimental evidence indicates that wave activity (with significant wave heights exceeding approximately 0.1 m) introduces wave-coherent motions and enhances near-surface turbulence, altering both the mean flow and turbulent momentum exchange. Therefore, the flow patterns and relative wind-speed differences reported here should be interpreted within the context of this idealized wave-free boundary condition. The influence of surface waves on the aerodynamic environment represents an important direction for future work, where the incorporation of dynamic wave-coupled boundary conditions would extend the model's applicability to a wider range of realistic aquatic settings. Additionally, the investigated model is constructed according to our experimental platform as a standalone aquavoltaic system, which cannot fully capture the complexity of large-scale arrays. When applied to large-scale solar power plants, the simulation results primarily characterize the aerodynamic behavior of the windward leading row, as well as those within arrays that have sufficient spacing under lateral wind conditions. As airflow moves into the interior of the array, the cumulative blockage and wake superposition from adjacent rows and support structures gradually restrict momentum transfer. Consequently, the internal wind speeds are expected to decrease, indicating that local channeling effects within the array will weaken, while overall flow deceleration becomes dominant. Despite these limitations, this work establishes a solid foundation for future research addressing scenarios involving more complex physical processes. Subsequent studies will incorporate 3-D water bodies and PV arrays into the model, integrating processes such as solar radiation absorption, natural convection, and air–water interface evaporation. Furthermore, coupled multiphysics approaches can be employed to simulate heat and mass transfer dynamics, enabling a holistic analysis of microclimate interactions within aquavoltaic systems.

CRediT authorship contribution statement

Haoran Chang: Writing – review & editing, Writing – original draft, Visualization, Software, Methodology, Investigation, Formal analysis, Conceptualization. **Peixin Dong:** Writing – review & editing, Writing – original draft, Visualization, Software, Methodology, Investigation. **Xin Wei:** Software, Investigation, Data curation. **Liutao Chen:** Writing – review & editing, Methodology, Investigation. **Hui Tang:** Writing – review & editing, Visualization, Methodology. **Zhe Wang:** Validation, Funding acquisition. **Su Guo:** Validation, Resources. **Mengying Li:** Writing – review & editing, Supervision, Project administration, Methodology, Funding acquisition.

Declaration of Generative AI and AI-assisted technologies in the writing process

During the preparation of this work, the authors used GPT-4 to improve language and readability. After using these tools, the authors reviewed and edited the content as needed and took full responsibility for the publication's content.

Declaration of competing interest

The authors declare that they have no known competing financial interests or personal relationships that could have appeared to influence the work reported in this paper.

Acknowledgment

The authors gratefully acknowledge the support of the Jiangsu Province Science and Technology Department (Project No. BZ2021057) and the substantial support from the Research Grants Council of the Hong Kong Special Administrative Region, China (Project No. C6003-22Y).

Appendix A. Derivation of the analytical formula for estimating relative wind speed

This section presents the theoretical derivation of the analytical formula, Eq. (5), for estimating the relative wind speed (u_r) over the water surface when a PV module is introduced. As illustrated in Fig. A1, in the absence of a PV module, the vertical velocity profile can be described using the power law. Hence, the relationship between the free-stream wind speed, u_a, and the boundary layer wind speed, u_b, is expressed as:

$$\frac{u_a}{u_b(\text{noPV})} = \left(\frac{h + L\sin\beta}{h_b}\right)^{\alpha} \tag{A.1}$$

When a PV module is introduced, it obstructs the airflow and alters the wind field, resulting in an equivalent wind speed, u_e, at the leading edge of the module, as illustrated in Fig. A2(a). Similarly, the vertical velocity profile from the water surface to the leading edge of the module can also be expressed using the power law:

$$\frac{u_e}{u_b(\text{withPV})} = \left(\frac{h}{h_b}\right)^{\alpha} \tag{A.2}$$

Consequently, the change in the boundary layer velocity due to the introduction of the PV module, quantified by u_r, can be expressed as:

$$u_r = \frac{u_b(\text{withPV})}{u_b(\text{noPV})} = \frac{u_e}{u_a}\left(\frac{h + L\sin\beta}{h}\right)^{\alpha} \tag{A.3}$$

To derive the analytical expression for u_r, it is first necessary to derive the expression for u_e. Assuming the air is incompressible, the fluid velocity field can be determined from the stream function, which is a scalar potential function. According to potential flow theory [38], when a thin body such as a PV module is introduced into a uniform free stream, the total potential is given by the superposition of the free stream potential and the perturbation potential induced by the module. Consequently, the equivalent velocity u_e can be expressed as the sum of the free-stream wind speed u_a and the disturbance velocity u'. As illustrated in Fig. A2(b), the airflow velocity encountering the PV module can be further decomposed into two components: a parallel component and a perpendicular component relative to the panel surface. The relationship between the equivalent velocity u_e and the free-stream velocity u_a is then:

$$\vec{u}_e = \vec{u}_w + \vec{v}_w \tag{A.4}$$

$$u_w = u_a\sin\beta' + u_w' \tag{A.5}$$

$$v_w = u_a\cos\beta' + v_w' \tag{A.6}$$

where β' is the incidence angle of the wind on the panel (replacing β to better capture the directional dependence in 3-D space), and u'_w and v'_w denote the perturbation velocities in the parallel and perpendicular directions, respectively.

Based on the velocity decomposition, the ratio of u_e and u_a can be expressed as:

$$\begin{aligned}\frac{u_e}{u_a} &= \sqrt{\frac{(u_a\sin\beta' + u'_w)^2 + (u_a\cos\beta' + v'_w)^2}{u_a^2}} \\ &= \sqrt{\frac{u_a^2 + (u'_w)^2 + (v'_w)^2 + 2u'_w u_a\sin\beta' + 2v'_w u_a\cos\beta'}{u_a^2}}\end{aligned} \tag{A.7}$$

Furthermore, since the perturbation velocity is small compared to the free-stream velocity, only the first-order terms are retained. The velocity component u_w along the PV surface is neglected, as it does not influence the airflow over the water surface. Consequently, Eq. (A.7) can be simplified to:

$$\frac{u_e}{u_a} = \sqrt{1 + \frac{2v'_w\cos\beta'}{u_a}} \tag{A.8}$$

Finally, substituting this result into Eq. (A.3) yields the complete formulation for the relative wind speed u_r. Defining $w = v'_w/u_a$ as the

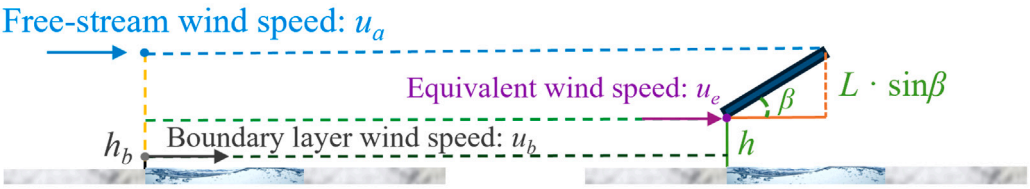

Fig. A1. Schematic of the system before and after obstructed by the PV module.

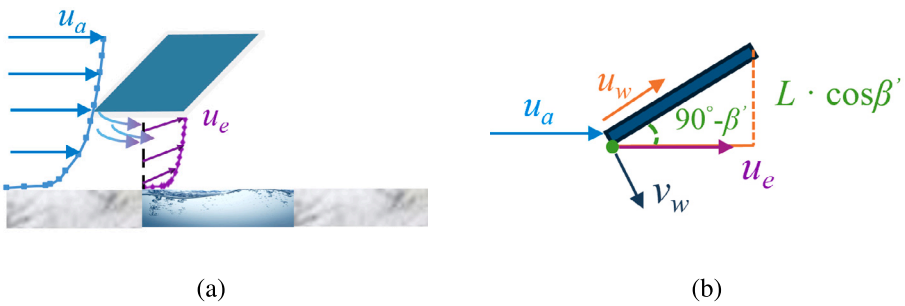

Fig. A2. (a) Relationship between free-stream and equivalent wind speeds. (b) Decomposition of incoming airflow at the leading edge of the PV module.

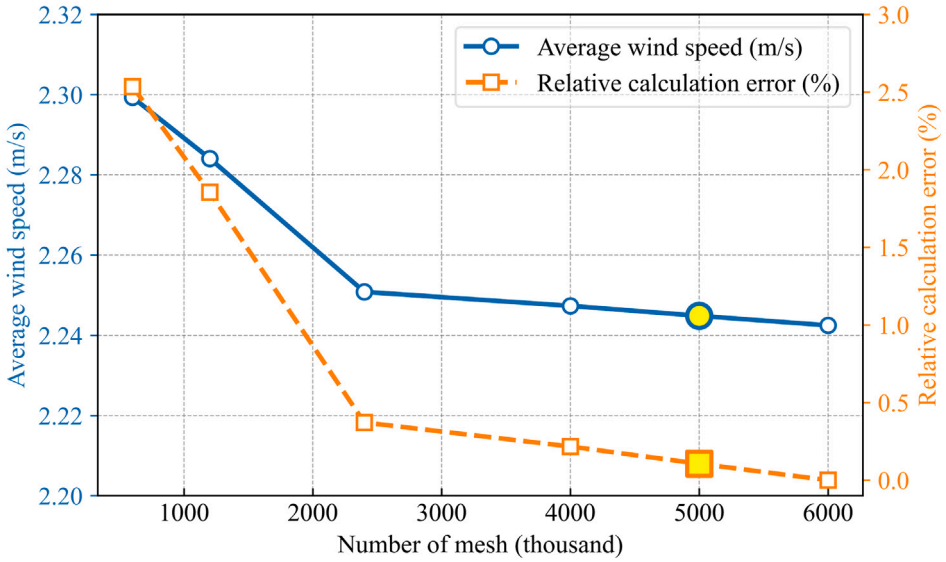

Fig. B1. Grid convergence test: average wind speed in the boundary layer and relative error with respect to mesh schemes.

ratio of the perturbation velocity normal to the PV module v'_w to u_a, the equation can be further expressed as:

$$u_r = \sqrt{1 + 2w\cos\beta'} \cdot \left(\frac{h + L\sin\beta}{h}\right)^{\alpha} \tag{A.9}$$

Appendix B. Grid convergence test

The computational domain is discretized with unstructured tetrahedral and prismatic grids, featuring refined boundary layer meshes at the ground, PV module, and water surface. The grid convergence test is conducted under the specified conditions listed in Table B.1, where the PV module produces pronounced aerodynamic effects.

Following the consistent meshing strategy, six progressively refined grid configurations are developed: mesh 1 (0.6 million elements, coarsest resolution), mesh 2 (1.2 million, coarser), mesh 3 (2.4 million, coarse), mesh 4 (4 million, fine), mesh 5 (5 million, finer), and mesh 6 (6 million, finest). The average wind speed within the velocity boundary layer above the water surface is used as the evaluation metric, as this region is particularly sensitive to aerodynamic disturbances induced by the PV module. To quantitatively assess mesh convergence, the relative error for each mesh was calculated with respect to the finest mesh (mesh 6), which is defined as the reference solution, as presented in Fig. B1.

The results show a monotonic convergence trend, with the predicted wind speed decreasing as the mesh resolution increases. When the total number of elements exceeds approximately 4 million, further mesh refinement yields negligible changes, and the relative error falls below 0.2%. Based on this convergence behavior, mesh 5 (approximately 5.1 million elements) was selected for all simulations as an optimal compromise between numerical accuracy and computational efficiency, as indicated by the yellow symbols. This level of numerical uncertainty is considered acceptable for resolving the coupled aerodynamic

Table B.1
Summary of testing conditions and selected meshing details.

Testing conditions		Meshing details	
Ambient temperature	25 °C	No. of elements	5058359
Water temperature	23 °C	Average element quality	0.76
Wind speed	2 m/s	No. of layers	22
Wind direction	180°	First layer thickness for ground and water surface	0.00012 m
PV height	0.5 m	Growth ratio	1.2
PV tilt angle	60°	First layer thickness for PV module surface	0.00012 m
PV azimuth angle	180°	Average y^+ for water surface	≈ 1.0

(a) (b) (c)

Fig. C1. Configuration of the experimental platform: (a) the SPV system, (b) nearby environmental weather station, and (c) water surface anemometer with mounting bracket.

interactions between the wind flow, PV module, and water surface investigated in this study.

Appendix C. Numerical model validation

The experimental matrix was designed to generate robust validation data for the numerical model characterizing wind–PV–water interactions, prioritizing physical representativeness and long-term operational stability over parametric variation. A fixed, small-scale experimental platform was constructed on a rooftop of Hohai University for this purpose. As illustrated in Fig. C1, the setup consists of a single PV module installed above a water pool at a representative tilt angle of 26°. This configuration ensures stable exposure to ambient wind and solar radiation while minimizing experimental uncertainty from geometric variables.

The water pool dimensions (210 cm (length) × 170 cm (width) × 15 cm (depth), wall thickness 13 cm) were selected to be sufficiently large relative to the module footprint. This ensures a region of fully developed flow beneath the module and minimizes edge effects from the pond boundaries. The platform is instrumented with microclimate monitoring sensors and an environmental weather station. A key feature is a custom-fabricated bracket that secures an anemometer 10 cm above the water surface at the pool's center, approximately 60 cm below the PV module.

Rather than actively varying geometric parameters, the validation leverages naturally varying environmental conditions – wind speed, direction, and ambient temperature – to sample a broad range of realistic operating states. To mitigate potential sensor degradation from prolonged outdoor exposure, data were filtered from the first three months of system operation. For direct model validation, field data from 10:00 to 13:00 on July 31, 2023, were selected during a period of relatively stable wind conditions and minimal temperature variation. To address the inherent high-frequency fluctuations in outdoor wind data, a 20 min moving average was applied to both wind speed and direction. This pre-processing yielded 10 temporally independent data points over the three-hour window, which were treated as repeated statistical realizations under quasi-steady inflow conditions—a conventional approach in outdoor microclimate studies where exact physical replication is impractical. Additionally, significant transient fluctuations were excluded to retain only the prevailing wind regime.

As shown in Fig. C2, the simulated wind speed at the anemometer location closely matches the measured trends. The slight overestimation observed falls within the ±3% sensor uncertainty band (approximately ±0.3 m/s) and can also be attributed to simplifications in the numerical model concerning PV support structures and pool boundaries. Overall, the comparison confirms the reliability and validity of the numerical model for capturing the prevailing flow dynamics in this experimental setup.

Appendix D. Assumption justifications

D.1. The effects of buoyancy and density variations under windy conditions

This study is conducted under the assumption that buoyancy effects and density variations are negligible for the wind conditions investigated. To quantitatively validate this assumption for our specific configuration, a coupled multiphysics simulation was performed for a representative case: a PV module with a 30° tilt, mounted 1 m above the water surface under a 2 m/s south wind. The boundary temperatures were set to 296.15 K for the water surface, 298.15 K for the ambient air, and 323.15 K for the PV module. The simulation solved for conjugate heat transfer and water-vapor transport in moist air, fully coupled with the turbulence model to capture thermally induced gradients and humidity diffusion in the near-surface airflow.

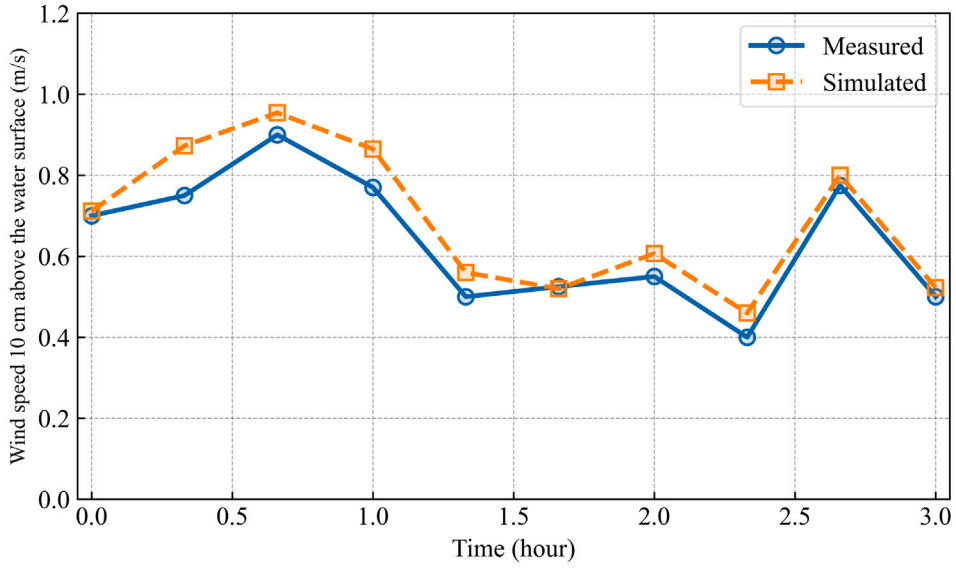

Fig. C2. Comparison between numerical results and experimental data.

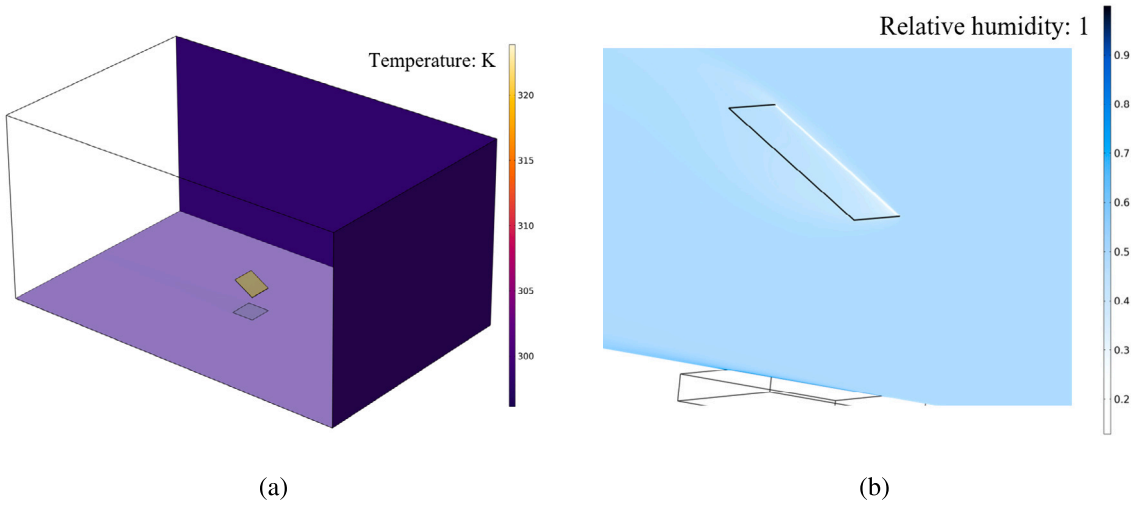

Fig. D1. The environmental temperature and humidity field resulting from the coupled heat and mass transfer simulation, (a) temperature field, (b) relative humidity field.

The resulting temperature and relative humidity (RH) fields for a baseline humidity of 0.5 are presented in Fig. D1. Due to the strong forced convection in this well-ventilated environment, water vapor does not accumulate; any increase in humidity is confined to a thin boundary layer immediately above the water surface. This confirms that humidity variation exerts a negligible influence on the bulk aerodynamic field.

A direct comparison of the velocity field is shown in Fig. D2 for different humidity levels. The airflow structure – including separation and recirculation patterns – exhibits virtually no discernible change when heat and mass transfer are included, compared to the isothermal, dry-air simulation. This underscores the absolute dominance of forced convection over weak buoyant effects in this configuration.

Quantitatively, the computed wind speeds at a fixed reference height are 1.9503 m/s for the uncoupled (isothermal) case, 1.9558 m/s for the coupled case at RH = 0.5, and 1.9559 m/s for the coupled case at RH = 0.9. The marginally higher velocities in the coupled simulations, on the order of 0.3%, are attributed to weak buoyant acceleration resulting from temperature-induced density gradients. This minimal deviation validates the initial simplification of neglecting buoyancy for the scope of this wind-driven study.

D.2. Comparative analysis with PV array scenarios

This study focuses on standalone PV systems in distributed settings. To demonstrate the applicability of the findings to centralized arrays and to quantify the differences, we constructed a small array of nine PV modules arranged in a 3 × 3 matrix and compared its airflow patterns with those of a single module, thereby providing insights for broader applications.

In this array setup, all modules are south-facing, with 10 cm lateral spacing between modules in the same row and 50 cm longitudinal gaps between rows, as illustrated in Fig. D3. Consistent with the standalone system, the modules are installed at a tilt angle of 30° and at a clearance height of 50 cm above the water surface. To facilitate a detailed analysis of the local flow field variations, we have numbered the modules from PV 1 to PV 9. Simulations were conducted at inlet wind speeds of 2 m/s and 4 m/s to ensure robustness, incorporating the four wind

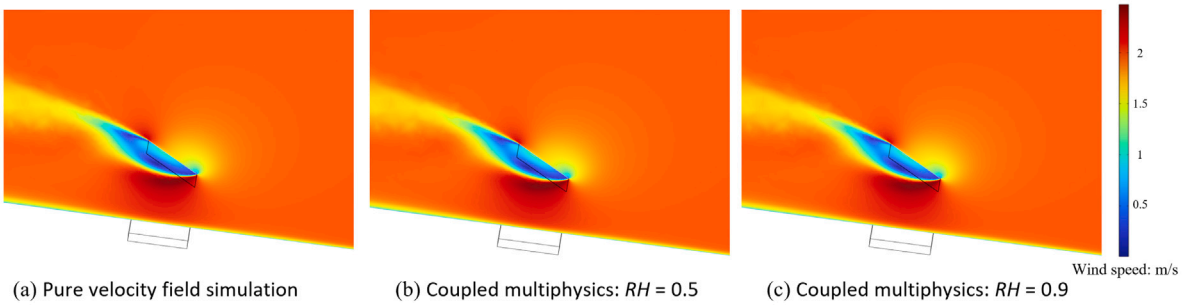

Fig. D2. Cross-sectional velocity fields along the module centerline under different physical field conditions: (a) pure velocity field; (b) coupled multiphysics at RH = 0.5; (c) coupled multiphysics at RH = 0.9.

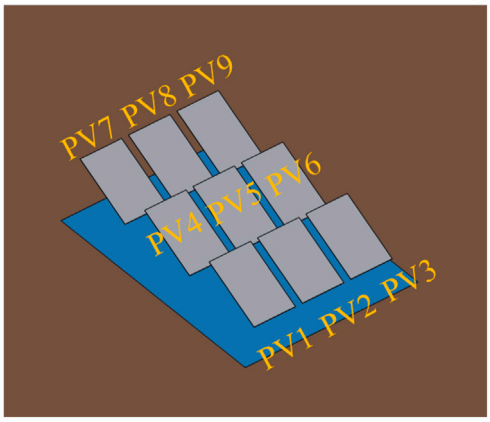

Fig. D3. CFD model for studying the wind field of a small PV array.

directions used in the standalone system study: south, southeast, north, and northeast.

The simulation results are presented in Fig. D4, which reveal distinct aerodynamic behaviors depending on the wind direction and the position of the modules within the array. Under the south wind, the "channeling acceleration effect" proposed in this study is clearly observable beneath the first row of PV modules (PV 1 to PV 3), which are the first to encounter the incoming airflow. However, as airflow progresses downstream, the acceleration effect beneath the subsequent rows gradually weakens. Similarly, under the north wind, the first row facing the wind (PV 7 to PV 9) exhibits a flow pattern consistent with the single-module findings, characterized by a combination of deceleration and local acceleration zones. In contrast, the other two rows exhibit substantial internal interference, leading to complex flow patterns, with an overall trend in which the wind speed above the water surface first increases and then decreases.

Interestingly, the results for the southeast and northeast winds present a different phenomenon. Because the wind approaches the array laterally in these cases, the airflow passes through the gaps with less obstruction compared to the direct north or south flows. As a result, the interference between rows is reduced, leading to similar flow patterns around each PV module. This suggests that, under oblique wind directions, the flow pattern generated by a single module is more uniformly preserved across the array compared to normal and reverse wind incidence.

To quantify the simulation results, we extracted the wind speed above the water surface beneath each PV module in the array from the numerical model and calculated the relative wind speed using the same reference wind speed as in the single-module study. Furthermore, the relative difference was calculated by comparing it with the relative wind speed at the corresponding position in the single-module scenario, as shown in Fig. D5.

The quantitative results enable an in-depth analysis of the phenomena observed in the flow field. For south and north winds, the relative wind speed under the leading row differs from the standalone case by less than 5%. In the south wind scenario, the speed drops sharply as the flow moves through the array, and this declining trend is expected to continue if additional rows are present. Under north wind, a deceleration effect occurs beneath PV 7 to 9, whereas an acceleration effect is observed beneath PV 4 to 6. As shown in Fig. D4(c), this behavior arises from the channeling effect that develops at the end of the first row and accelerates the flow into the second row, although the effect is weaker than in the south wind case and gradually diminishes downstream.

Regarding lateral winds, the distribution of differences is fairly uniform, with variations across all PV modules remaining below 10%. However, modules further downstream (e.g., PV 7 and PV 4 under southeast winds) diverge from the general trend, suggesting that module interaction strengthens as the wind flows through the array. This phenomenon arises because the 50 cm row spacing used in this setup represents a very dense layout. In real installations, where system maintenance or aquaculture activities must be accommodated, the spacing is typically much larger, leading to significantly weaker interactions between modules.

These findings indicate that the results of the standalone system are applicable to the leading row of the PV array under north/south winds. As airflow penetrates deeper into the array, wake interactions and blockage effects begin to dampen the local wind speed, causing a gradual decrease. Under lateral winds, if the array is not excessively dense, the results remain valid for a larger portion of the PV modules. Furthermore, the simulation results reveal that wind field variations over water within an array involve complex interactions among modules, leading to significant differences in flow patterns between rows. These variations are strongly influenced by the structural layout of the array; for example, increasing the row spacing produces a flow field that more closely resembles that of a single module. Consequently, diverse array configurations may yield varying outcomes, highlighting the need for further research.

Data availability

The data in this study will be made available upon reasonable request.

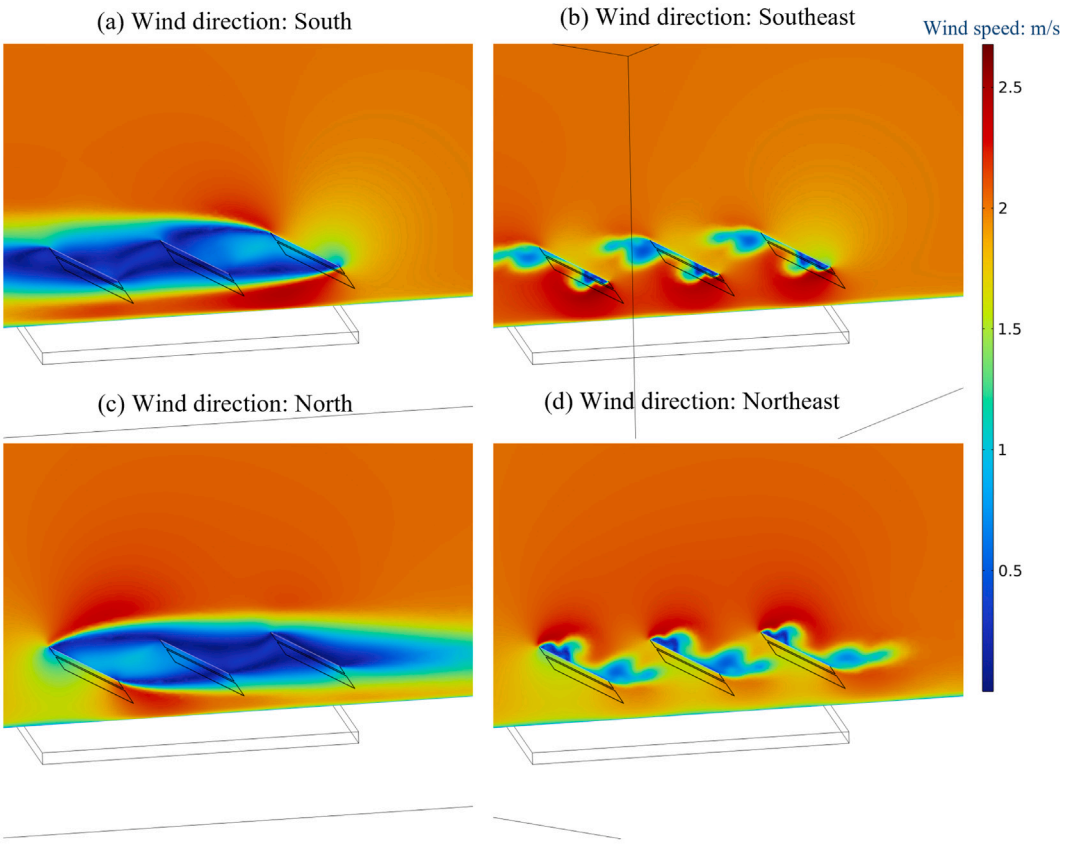

Fig. D4. Cross-sectional velocity field along the center of the array at an inlet wind speed of 2 m/s under different wind directions: (a) south, (b) southeast, (c) north, and (d) northeast.

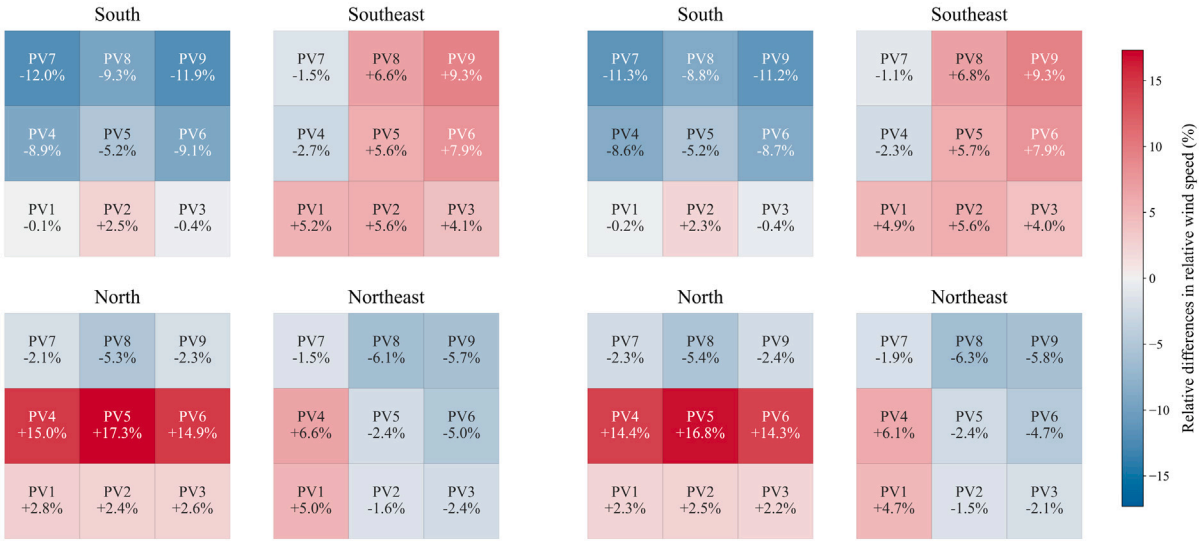

(a) Inlet wind speed: 2 m/s

(b) Inlet wind speed: 4 m/s

Fig. D5. The relative differences in local relative wind speed beneath each module within the array compared to that of the standalone module at an inlet wind speed of (a) 2 m/s and (b) 4 m/s.

References

[1] Y. Feng, J. Zhang, Y. Geng, S. Jin, Z. Zhu, Z. Liang, Explaining and modeling the reduction effect of low-carbon energy transition on energy intensity: Empirical evidence from global data, Energy 281 (2023) 128276.

[2] Q. Hassan, P. Viktor, T.J. Al-Musawi, B.M. Ali, S. Algburi, H.M. Alzoubi, A.K. Al-Jiboory, A.Z. Sameen, H.M. Salman, M. Jaszczur, The renewable energy role in the global energy Transformations, Renew. Energy Focus. 48 (2024) 100545.

[3] M. Kumar, A. Kumar, R. Gupta, Comparative degradation analysis of different photovoltaic technologies on experimentally simulated water bodies and estimation of evaporation loss reduction, Prog. Photovolt., Res. Appl. 29 (3) (2021) 357–378.

[4] L. Chen, S. Zhang, I. Cheng, H. Chang, F. Chen, M. Li, Z. Wang, The resilience

paradox of rooftop PV: Building cooling penalties and heat risks, Build. Environ. (2025) 113233.
[5] W. Wan, X. Zhang, Z. Sun, X. Zhou, Y. He, T. Lv, H. Hou, Assessing the impact of photovoltaic system construction on green environment in China using an interpretable machine learning approach, Renew. Energy (2025) 124120.
[6] H. Guo, X. Wang, B. Liu, Z. Chan, Z. Pan, L. Chen, Q. Xi, W. Zhu, J. Wu, G. Cao, et al., Global trends and evolution of aquavoltaics in sustainable aquaculture and energy generation, Renew. Energy (2025) 123864.
[7] A. Ghosh, A comprehensive review of water based PV: Flotavoltaics, under water, offshore & canal top, Ocean Eng. 281 (2023) 115044.
[8] J. Hu, K. Teng, C. Li, X. Li, J. Wang, P.D. Lund, Review of recent water photovoltaics development, Oxf. Open Energy 2 (2023) oiad005.
[9] S. Benjamins, B. Williamson, S.-L. Billing, Z. Yuan, M. Collu, C. Fox, L. Hobbs, E.A. Masden, E.J. Cottier-Cook, B. Wilson, Potential environmental impacts of floating solar photovoltaic systems, Renew. Sustain. Energy Rev. 199 (2024) 114463.
[10] M. Kumar, A. Kumar, Experimental characterization of the performance of different photovoltaic technologies on water bodies, Prog. Photovolt., Res. Appl. 28 (1) (2020) 25–48.
[11] L. Chen, Z. Lin, Q. Zhou, S. Zhang, M. Li, Z. Wang, Impacts of photovoltaics and integrated green roofs on urban climate: Experimental insights for urban land surface modelling, Renew. Sustain. Energy Rev. 217 (2025) 115709.
[12] A. Minoofar, A. Zandi, A. Gholami, Precise prediction models for floating and land-based Photovoltaics: Comparative analysis for advancing sustainable energy and water management solutions, Renew. Energy (2025) 123781.
[13] J. Sun, Y. He, X. Li, Z. Lu, X. Yang, CFD simulations for layout optimal design for ground-mounted photovoltaic panel arrays, J. Wind Eng. Ind. Aerodyn. 242 (2023) 105558.
[14] C.M. Jubayer, H. Hangan, A numerical approach to the investigation of wind loading on an array of ground mounted solar photovoltaic (PV) panels, J. Wind Eng. Ind. Aerodyn. 153 (2016) 60–70.
[15] W. Hu, X. Li, J. Wang, Z. Tian, B. Zhou, J. Wu, R. Li, W. Li, N. Ma, J. Kang, et al., Experimental research on the convective heat transfer coefficient of photovoltaic panel, Renew. Energy 185 (2022) 820–826.
[16] A. Vasel, F. Iakovidis, The effect of wind direction on the performance of solar PV plants, Energy Convers. Manage. 153 (2017) 455–461.
[17] E. Kaplani, S. Kaplanis, Thermal modelling and experimental assessment of the dependence of PV module temperature on wind velocity and direction, module orientation and inclination, Sol. Energy 107 (2014) 443–460.
[18] M.J. Wilson, M.C. Paul, Effect of mounting geometry on convection occurring under a photovoltaic panel and the corresponding efficiency using CFD, Sol. Energy 85 (10) (2011) 2540–2550.
[19] A. Djalab, Z. Djalab, A. El Hammoumi, G.M. Tina, S. Motahhir, A.A. Laouid, A comprehensive review of floating photovoltaic systems: Tech advances, marine environmental influences on offshore PV systems, and economic feasibility analysis, Sol. Energy 277 (2024) 112711.
[20] T. Kjeldstad, V.S. Nysted, M. Kumar, S. Oliveira-Pinto, G. Otnes, D. Lindholm, J. Selj, The performance and amphibious operation potential of a new floating photovoltaic technology, Sol. Energy 239 (2022) 242–251.
[21] I. Peters, A. Nobre, Deciphering the thermal behavior of floating photovoltaic installations, Sol. Energy Adv. 2 (2022) 100007.
[22] C. Ramanan, K.H. Lim, J.C. Kurnia, Thermal behavior of floating photovoltaics: A comparison of performance at varying heights and benchmarking against land-based photovoltaics, Appl. Energy 388 (2025) 125642.
[23] C. Ramanan, K.H. Lim, J.C. Kurnia, S. Roy, B.J. Bora, B.J. Medhi, Design study on the parameters influencing the performance of floating solar PV, Renew. Energy 223 (2024) 120064.
[24] V. Vidović, G. Krajačić, N. Matak, G. Stunjek, M. Mimica, Review of the potentials for implementation of floating solar panels on lakes and water reservoirs, Renew. Sustain. Energy Rev. 178 (2023) 113237.
[25] S.E. Baradei, M.A. Sadeq, Effect of solar canals on evaporation, water quality, and power production: An optimization study, Water 12 (8) (2020) 2103.
[26] H.P. Hamedani, S. Gorjian, B. Ghobadian, H. Mokhtarzadeh, Development and experimental performance evaluation of a small-scale aquavoltaic system for microalgae production, Results Eng. 24 (2024) 102919.
[27] P.-A. Château, R.F. Wunderlich, T.-W. Wang, H.-T. Lai, C.-C. Chen, F.-J. Chang, Mathematical modeling suggests high potential for the deployment of floating photovoltaic on fish ponds, Sci. Total Environ. 687 (2019) 654–666.
[28] C. Hermann, F. Dahlke, U. Focken, M. Trommsdorff, Aquavoltaics: Dual use of natural and artificial water bodies for aquaculture and solar power generation, in: Solar Energy Advancements in Agriculture and Food Production Systems, Elsevier, 2022, pp. 211–236.
[29] Z. Akhtar, M. Lalwani, K. Rao, Estimation of energy potential and evaporation in 20 lakes with FPV in Rajasthan India, Renew. Energy (2025) 124297.
[30] K. Ilgen, D. Schindler, S. Wieland, J. Lange, The impact of floating photovoltaic power plants on lake water temperature and stratification, Sci. Rep. 13 (1) (2023) 7932.
[31] D. Waterworth, A. Armstrong, Southerly winds increase the electricity generated by solar photovoltaic systems, Sol. Energy 202 (2020) 123–135.
[32] R.N. Pratt, G.A. Kopp, Velocity measurements around low-profile, tilted, solar arrays mounted on large flat-roofs, for wall normal wind directions, J. Wind Eng. Ind. Aerodyn. 123 (2013) 226–238.
[33] A.M. Aly, G. Bitsuamlak, Aerodynamics of ground-mounted solar panels: Test model scale effects, J. Wind Eng. Ind. Aerodyn. 123 (2013) 250–260.
[34] K. Mehta, M.J. Shah, W. Zörner, Agri-PV (agrivoltaics) in developing countries: advancing sustainable farming to address the water–energy–food nexus, Energies 17 (17) (2024) 4440.
[35] T. Yunus Khan, M.E.M. Soudagar, M. Kanchan, A. Afzal, N.R. Banapurmath, N. Akram, S.D. Mane, K. Shahapurkar, Optimum location and influence of tilt angle on performance of solar PV panels, J. Therm. Anal. Calorim. 141 (1) (2020) 511–532.
[36] A. Sohail, M.S. Rusdi, M.Z. Abdullah, S.M. Sultan, Numerical investigation of the thermal performance of PV system under variable wind speeds and ambient temperatures in the tropical climate of Malaysia, Green Technol. Sustain. (2025) 100210.
[37] Z. Li, C. Hu, H. Wu, S. Wang, R. Te, X. Luan, Research on wind pressure distribution of large-scale tracking photovoltaic power generation array based on supercomputing, Acta Energ. Sol. Sin. 44 (2023) 242251.
[38] E.L. Houghton, P.W. Carpenter, Aerodynamics for Engineering Students, Elsevier, 2003.
[39] H. Torita, H. Satou, Relationship between shelterbelt structure and mean wind reduction, Agricult. Forest. Meterol. 145 (3–4) (2007) 186–194.
[40] J. Franke, A. Hellsten, H. Schlünzen, B. Carissimo, The best practise guideline for the CFD simulation of flows in the urban environment: an outcome of COST 732, in: The Fifth International Symposium on Computational Wind Engineering, CWE2010, 2010, pp. 1–10.
[41] M. Shademan, A. Naghib-Lahouti, Effects of aspect ratio and inclination angle on aerodynamic loads of a flat plate, Adv. Aerodyn. 2 (2020) 1–23.
[42] F.P. Incropera, D.P. DeWitt, T.L. Bergman, A.S. Lavine, et al., Fundamentals of heat and mass transfer, vol. 6, Wiley New York, 1996.
[43] F. Castellani, A. Eltayesh, F. Natili, T. Tocci, M. Becchetti, L. Capponi, D. Astolfi, G. Rossi, Wind flow characterisation over a PV module through URANS simulations and wind tunnel optical flow methods, Energies 14 (20) (2021) 6546.
[44] S. Nižetić, F. Grubišić-Čabo, I. Marinić-Kragić, A.M. Papadopoulos, Experimental and numerical investigation of a backside convective cooling mechanism on photovoltaic panels, Energy 111 (2016) 211–225.
[45] Q. Zhou, P. Dong, M. Li, Z. Wang, Analyzing the interactions between photovoltaic system and its ambient environment using CFD techniques: A review, Energy Build. 296 (2023) 113394.
[46] P. Dong, H. Chang, N. Deng, S. Guo, M. Li, Multiphysics modelling of open-water evaporation: Quantifying the natural convection effects of water, Appl. Therm. Eng. (2025) 126964.
[47] F. Bontempo Scavo, G.M. Tina, A. Gagliano, S. Nižetić, An assessment study of evaporation rate models on a water basin with floating photovoltaic plants, Int. J. Energy Res. 45 (1) (2021) 167–188.
[48] J.H. Lienhard, Heat transfer in flat-plate boundary layers: A correlation for laminar, transitional, and turbulent flow, J. Heat Transf. 142 (6) (2020) 061805.